

ISSN: (Print) (Online) Journal homepage: www.tandfonline.com/journals/tbsd20

Structure-activity relationship of peptide conjugates derived from BP100 and insights into their interactions with lipid membranes by NMR and MD simulations

Gerard Riesco-Llach, Àngel Oliveras, Sergio Gil-Caballero, Esther Badosa, Anna Bonaterra, Emilio Montesinos, Ferran Feixas, Marta Planas & Lidia Feliu

To cite this article: Gerard Riesco-Llach, Àngel Oliveras, Sergio Gil-Caballero, Esther Badosa, Anna Bonaterra, Emilio Montesinos, Ferran Feixas, Marta Planas & Lidia Feliu (31 Jan 2025): Structure-activity relationship of peptide conjugates derived from BP100 and insights into their interactions with lipid membranes by NMR and MD simulations, Journal of Biomolecular Structure and Dynamics, DOI: [10.1080/07391102.2025.2458328](https://doi.org/10.1080/07391102.2025.2458328)

To link to this article: <https://doi.org/10.1080/07391102.2025.2458328>



© 2025 The Author(s). Published by Informa UK Limited, trading as Taylor & Francis Group



[View supplementary material](#)



Published online: 31 Jan 2025.



[Submit your article to this journal](#)



Article views: 43



[View related articles](#)



[View Crossmark data](#)

Structure-activity relationship of peptide conjugates derived from BP100 and insights into their interactions with lipid membranes by NMR and MD simulations

Gerard Riesco-Llach^a, Àngel Oliveras^a, Sergio Gil-Caballero^b, Esther Badosa^c, Anna Bonaterra^c, Emilio Montesinos^c, Ferran Feixas^d, Marta Planas^a, and Lidia Feliu^a

^aLIPPSO, Department of Chemistry, Campus Montilivi, Universitat de Girona, Girona, Spain; ^bServeis Tècnics de Recerca (NMR), Universitat de Girona, Parc Científic i Tecnològic de la UdG, Girona, Spain; ^cLaboratory of Plant Pathology, Institute of Food and Agricultural Technology-CIDSAV-XaRTA, Campus Montilivi, Universitat de Girona, Girona, Spain; ^dInstitut de Química Computacional i Catàlisi and Departament de Química, Universitat de Girona, Campus Montilivi, Girona, Spain

ABSTRACT

Antimicrobial and plant defence elicitor peptides have received attention on last decades as novel tools to combat bacterial plant diseases. We previously reported a library of peptide conjugates resulting from the combination of an antimicrobial peptide (**BP16**, **BP143**, **BP387** or **BP475**) and a plant defence elicitor sequence (**fig15**, **BP13**, **Pep13** or **PIP1**). From this library, we selected a set of 14 peptide conjugates including both highly and poorly active sequences and we performed a structure-activity relationship study by NMR and MD simulations. Analysis of their structure by NMR in 30% TFE-d₃ and in zwitterionic DPC-d₃₈ and anionic SDS-d₂₅ micelles showed that the presence of an α -helix fragment together with a flexible random coil can be related to a high antibacterial activity and a low hemolysis. In contrast, the sequences with a rigid α -helix structure were low active and highly hemolytic. PRE-NMR experiments in presence of MnCl₂ and 16-DSA revealed that the highly active peptides **fig15-BP475** and **BP100-Pep13** interacted stronger with DPC-d₃₈ micelles than the low active peptide **BP13-BP16**. In the two former sequences this interaction took place through the α -helix region. From GaMD simulations of **BP100-Pep13** conducted in membranes composed of anionic DPPG lipids, after its electrostatic interaction, the peptide flipped and the hydrophobic residues were faced to the membrane triggering its insertion and also causing membrane thinning. Thus, the flexibility and moderate cationicity of **BP100-Pep13** seem to be crucial for its biological activity. These findings can help to establish the guidelines for future rational design of **BP100** derivatives.

ARTICLE HISTORY

Received 17 January 2024
Accepted 7 May 2024

KEYWORDS




Antimicrobial peptides;
secondary structure;
mechanism; computational
studies; micelles


1. Introduction

Agriculture is nowadays facing major challenges mainly related to the increasing population growth, the climate change, the devastation caused by plant pathogens and the scarcity of pesticides that can be used according to the actual regulations. In this context, antimicrobial peptides (AMPs) have aroused great interest as potential alternative of conventional pesticides due to their unique structural and biological properties (Erdem Büyükkiraz & Kesmen, 2022; Lobo & Boto, 2022; Luo et al., 2023). These bioactive small proteins are naturally produced by organisms from both the prokaryotic and eukaryotic organisms, including microorganisms, plants, insects, amphibians and mammals, among others. AMPs display a broad spectrum of activity against Gram-positive and Gram-negative bacteria, fungi, and viruses (Chen & Lu, 2020; Lei et al., 2019; Mahlapuu et al., 2020).

They are generally cationic short sequences, containing around 50% of hydrophobic residues and with a linear structure that can adopt an amphipathic α -helix. Although they can act through multiple targets and mechanisms of action, their main target is the bacterial membrane. It is well known that their cationicity allows their electrostatic interaction before the hydrophobic face is inserted into the membrane bilayer (Ciurac et al., 2019; Li et al., 2017; Talapko et al., 2022). This mode of action contributes to avoid the emergence of resistance in target pathogens (Liu et al., 2021; Magana et al., 2020; Xuan et al., 2023).

Among the large list of known AMPs, KKLFLKILKYL-NH₂ (**BP100**) is a linear undecapeptide first identified in our group with high activity against gram negative plant pathogenic bacteria, including *Erwinia amylovora*, two *Pseudomonas* species and three *Xanthomonas* species

CONTACT Marta Planas  marta.planas@udg.edu; Lidia Feliu  lidia.feliu@udg.edu  LIPPSO, Department of Chemistry, Campus Montilivi, Universitat de Girona, Girona, Spain; Ferran Feixas  ferran.feixas@udg.edu  Institut de Química Computacional i Catàlisi and Departament de Química, Universitat de Girona, Campus Montilivi, Girona, Spain

 Supplemental data for this article can be accessed online at <https://doi.org/10.1080/07391102.2025.2458328>.

© 2025 The Author(s). Published by Informa UK Limited, trading as Taylor & Francis Group
This is an Open Access article distributed under the terms of the Creative Commons Attribution-NonCommercial-NoDerivatives License (<http://creativecommons.org/licenses/by-nc-nd/4.0/>), which permits non-commercial re-use, distribution, and reproduction in any medium, provided the original work is properly cited, and is not altered, transformed, or built upon in any way. The terms on which this article has been published allow the posting of the Accepted Manuscript in a repository by the author(s) or with their consent.

(Badosa et al., 2007). In addition, **BP100** is low hemolytic and phytotoxic. Since our findings, this peptide has been investigated by many other research groups for other applications (Devi et al., 2022; Eales et al., 2018; Eggenberger et al., 2011; Miyamoto et al., 2022; Oddo et al., 2016; Souza et al., 2020; Torres et al., 2019; Yilmaz et al., 2021; Zhang et al., 2017). In our group, we have developed **BP100** derivatives to optimize its biological activity in the field of plant diseases, such as sequences bearing D-amino acids or a fatty acid chain, or peptide conjugates (Badosa et al., 2022). In particular, we have recently prepared a collection of thirty peptide conjugates resulting from the conjugation of an AMP (**BP16**, **BP100**, **BP143**, **KSL-W**, **BP387** or **BP475**) at the N- or C-terminus of a plant defence elicitor peptide (**flg15**, **BP13**, **Pep13** or **PIP1**) (Oliveras et al., 2022). Among the peptide conjugates with the best biological profile, **BP100-Pep13**, **Pep13-BP100** and **BP475-PIP1** stand out for their MIC values (between 0.8 and 12.5 μM) against all the tested bacteria. In addition, **flg15-BP475** and **PIP1-BP475** show MIC $<0.8\mu\text{M}$ against two *Xanthomonas* species. All these peptide conjugates are low hemolytic. In this study it has been observed that the order of the monomers in the peptide conjugates influences both the antibacterial and hemolytic activities.

The secondary structure of **BP100** as well as its interaction with lipid membranes has been thoroughly investigated by different research groups using circular dichroism (CD), oriented CD (OCD), nuclear magnetic resonance (NMR) and molecular dynamics (MD) simulations. It has been found that this peptide is highly α -helical in the presence of membranes. OCD and NMR experiments provided evidence that the **BP100** helix is oriented essentially flat on the bilayer surface (S-state) or slightly tilted within the membrane, while also exhibiting remarkable mobility (Wadhvani et al., 2014; Zamora-Carreras et al., 2016). Solid state ^{15}N and ^2H NMR studies in model membranes of different lipid composition pointed out that whereas the azimuthal rotation angle remains constant, the tilt angle and the dynamic fluctuations of the peptide depends on its concentration and on the spontaneous lipid curvature (Zamora-Carreras et al., 2016). These experiments have also shown that the C-terminus of **BP100** can get inserted into the hydrophobic core of the membrane while the N-terminus remains on the membrane surface. From ^2H NMR and grazing incidence small angle X-ray scattering (GISAXS) it has been concluded that **BP100** induces membrane thinning, as expected for amphiphilic sequences that interact almost parallel with the membrane (Grage et al., 2016). All these results together with the short length of **BP100** rule out the formation of pores. Instead, they suggest a carpet mechanism, wherein peptide binding to the outer monolayer surface induces enhanced membrane permeabilization, ultimately resulting in bacterial cell death. More recently, further OCD and NMR experiments carried out by Strandberg et al. varying the lipid length, peptide concentration and temperature reveal that **BP100** can adopt a stable upright transmembrane orientation under suitable conditions (I-state) (Strandberg et al., 2023).

MD simulations have allowed the description of the molecular interactions of **BP100** with the membrane at the atomic level. These simulations are in accordance with the above OCD and NMR experimental observations. **BP100** has a random coil conformation in a water environment and folds into α -helix upon interacting with negatively charged membranes (Park et al., 2019). A 8 μs MD simulation in DMPC bilayers has shown that **BP100** remains in the surface of the membrane, slightly tilted and with its C-terminus inserted into the bilayer (Wang et al., 2014). Performing longer MD simulations in more complex model membranes it has been observed that, initially, the polar residues of the α -helix are in contact with the membrane and the apolar face exposed to solvent. Afterwards, **BP100** flips leaving the hydrophobic residues buried into the core of the bilayer (Park et al., 2019). Franco et al. have described that this insertion increases the conformational dynamism of the hydrophobic chains of the membrane resulting in a negative curvature, a reduction of the lipid lateral diffusion and a local membrane thinning (Franco et al., 2022). In addition, MD simulations carried out by Strandberg et al. suggest that the I-state observed by NMR in several conditions could be stabilized by Lys side chains snorkelling to remain in a polar environment (Strandberg et al., 2023).

Even though the mechanism of action of **BP100** was studied by several groups, to the best of our knowledge similar studies had not been undertaken with **BP100** derivatives. As described above, we have identified peptide conjugates with an interesting biological activity profile to be used as plant protection products. Understanding the mode of action of these peptide conjugates would help in the design of new sequences with enhanced properties. Thus, herein, we selected peptide conjugates with a distinct activity and performed a comprehensive study of their activity-structure relationship. Their secondary structure and their localization in micelles were studied by NMR. In addition, computational studies based on molecular dynamics (MD) and enhanced sampling simulations were conducted to explore the conformational ensemble of the peptide conjugates as well as the molecular basis of their interaction with membranes. The results provided evidence for a correlation between the conformation, membrane interaction and biological activity.

2. Results

2.1. Selection of peptide conjugates

Peptide conjugates were selected from a previously described library of sequences resulting from the conjugation of an AMP with a sequence able to induce plant defence responses (Oliveras et al., 2022). This library included sequences active against the plant pathogenic bacteria *Erwinia amylovora* (Ea), *Xanthomonas arboricola* pv. pruni (Xap), *Xanthomonas fragariae* (Xf), *Xanthomonas axonopodis* pv. vesicatoria (Xav), *Pseudomonas syringae* pv. actinidiae (Psa) and *Pseudomonas syringae* pv. syringae (Pss), and with low hemolysis.

From this library, we selected 14 sequences with a distinct biological activity profile and which contain the AMP **BP100**

or a derivative (**BP16**, **BP143**, **BP387** or **BP475**) at the N- or the C-terminus of the plant defence elicitor peptide (**flg15**, **BP13**, **Pep13** or **PIP-1**) (Table 1). Compared to **BP100**, **BP16** contains a Lys¹⁰, **BP143** a D-Phe⁴, **BP387** a Lys⁸(COC₃H₇), and **BP475** a D-Phe⁴ and a Lys¹⁰(COC₃H₇). This set of peptide conjugates would allow to study the relationship between their secondary structure and their biological activity as well as the influence of the order of the two monomers in both the secondary structure and the biological activity. In particular, these selected sequences included ten highly active peptide conjugates with MIC <12.5 μM against five or six pathogens; two moderately active peptides with MIC <12.5 μM against three or four pathogens; and two poorly active sequences with MIC <12.5 μM against two pathogens. Regarding the hemolysis, those peptide conjugates with high and moderate activity were low hemolytic (≤28% hemolysis at 150 μM) and the least active ones exhibited high hemolysis (≥86% at 150 μM). The activity of the 14 selected peptide conjugates is summarized in Table 2.

2.2. Analysis of the secondary structure of peptide conjugates in presence of TFE

Peptide conjugates were characterized by NMR, because this technique is very useful to describe in atomic detail the three-dimensional structure of peptides in membrane

Table 1. Selected peptide conjugates.

Peptide	Sequence ^a
BP475-flg15	Ac-KKLFKKILKK(COC ₃ H ₇)-L-RINSAKDDAAGLQIA-OH
flg15-BP475	Ac-RINSAKDDAAGLQIA-KKLFKKILKK(COC ₃ H ₇)-L-NH ₂
BP387-flg15	Ac-KKLFKKIK(COC ₃ H ₇)-KYL-RINSAKDDAAGLQIA-OH
flg15-BP387	Ac-RINSAKDDAAGLQIA-KKLFKKIK(COC ₃ H ₇)-KYL-NH ₂
PIP1-BP475	Ac-YGIHHTH-KKLFKKILKK(COC ₃ H ₇)-L-NH ₂
BP475-PIP1	Ac-KKLFKKILKK(COC ₃ H ₇)-L-YGIHHTH-NH ₂
Pep13-BP100	VWNQPVGRGFKVYE-KKLFKKILKYL-NH ₂
BP100-Pep13	KKLFKKILKYL-VWNQPVGRGFKVYE-OH
Pep13-BP143	VWNQPVGRGFKVYE-KKLFKKILKYL-NH ₂
BP143-Pep13	KKLFKKILKYL-VWNQPVGRGFKVYE-OH
Pep13-BP16	VWNQPVGRGFKVYE-KKLFKKILKYL-NH ₂
BP16-Pep13	KKLFKKILKYL-VWNQPVGRGFKVYE-OH
BP13-BP16	FKLFKKILKVL-KKLFKKILKYL-NH ₂
BP16-BP13	KKLFKKILKYL-KKLFKKILKYL-NH ₂

^aCOC₃H₇, butanoyl; lower case letters correspond to D-amino acids.

environments. Their characterization was performed in aqueous solution in presence of 30% 2,2,2-trifluoroethanol-d₃ (TFE-d₃). Trifluoroethanol is a widely used cosolvent in NMR studies to mimic the hydrophobic environment of bacterial membranes and elucidate the conformation of AMPs (Buck, 1998; Mercurio et al., 2019; Santiveri et al., 2005). It is suggested that it acts lowering the hydrogen bond interaction with the solvent thereby promoting the intramolecular hydrogen bonds responsible for the stabilization of the secondary structure of the peptide (Sönnichsen et al., 1992).

The full assignment of ¹H, ¹³C, and ¹⁵N signals and of the primary structure was accomplished by the combination of nuclear Overhauser effect (NOE) correlations, H_{α(i)}-HN_(i+1) interresidue correlations, and total correlation spectroscopy (TOCSY) H_{α(i)}-HN_(i) intraresidue correlations. The secondary structure was predicted by the chemical shift index (CSI3.0) based on the ¹H-, ¹³C- and ¹⁵N- chemical shifts (Supporting Information) and was confirmed by NOESY and TOCSY correlations. The chemical shift deviation (Δδ, ppm) for ¹H_α and ¹³C_α from random coil shifts were calculated and, in addition, the percentage of α-helix population was determined by comparing the experimental Δδ_{H_α} with the averaged Δδ_{H_α} described for α-helix proteins (-0.39 ppm) (Supporting Information) (Vila et al., 2000; Wishart et al., 1991; Zamora-Carreras et al., 2015). The schematic representation of the secondary structure of the 14 peptide conjugates is depicted in Figure 1. A summary of NOEs for representative peptide conjugates is included in Figure 2.

The four peptide conjugates derived from the combination of the elicitor peptide **flg15** with the antimicrobial peptide **BP387** or **BP475** showed a percentage of α-helix population ranging from 62 to 69%. This α-helix mainly involves the residues of the antimicrobial peptide irrespective of its position at the N- or C-terminus of the conjugate. Accordingly, NOESY spectra of these four peptide conjugates confirmed a random coil conformation for most of the residues corresponding to the **flg15** moiety and that the antimicrobial fragment adopted an α-helix. For instance, as depicted in Figure 2, the NOESY spectra of **flg15-BP475** exhibited only the presence of sequential NN(i, i + 1), αN(i, i + 1) and βN(i, i + 1) NOEs for residues 1 to 11. In contrast,

Table 2. Antibacterial activity (MIC) and hemolysis of the selected peptide conjugates.

Peptide	MIC (μM)						Hemolytic activity (%) ^b
	<i>Ea</i> ^a	<i>Xap</i> ^a	<i>Xf</i> ^a	<i>Xav</i> ^a	<i>Psa</i> ^a	<i>Pss</i> ^a	
flg15-BP475	3.1–6.2	<0.8	6.2–12.5	<0.8	3.1–6.2	12.5–25	28 ± 2.3
BP475-flg15	12.5–25	1.6–3.1	25–50	3.1–6.2	3.1–6.2	6.2–12.5	0 ± 0.2
flg15-BP387	12.5–25	0.8–1.6	3.1–6.2	0.8–1.6	12.5–25	12.5–25	15 ± 1.6
BP387-flg15	25–50	1.6–3.1	6.2–12.5	3.1–6.2	6.2–12.5	3.1–6.2	5 ± 0.9
PIP1-BP475	3.1–6.2	<0.8	12.5–25	<0.8	1.6–3.1	3.1–6.2	11 ± 0.5
BP475-PIP1	3.1–6.2	0.8–1.6	1.6–3.1	3.1–6.2	1.6–3.1	6.2–12.5	18 ± 1.4
Pep13-BP16	6.2–12.5	0.8–1.6	3.1–6.2	0.8–1.6	1.6–3.1	6.2–12.5	3 ± 0.2
BP16-Pep13	6.2–12.5	0.8–1.6	1.6–3.1	1.6–3.1	1.6–3.1	1.6–3.1	1 ± 0.3
BP100-Pep13	0.8–1.6	1.6–3.1	3.1–6.2	1.6–3.1	0.8–1.6	1.6–3.1	12 ± 1.1
Pep13-BP100	6.2–12.5	0.8–1.6	6.2–12.5	0.8–1.6	3.1–6.2	6.2–12.5	25 ± 2.4
BP143-Pep13	1.6–3.1	1.6–3.1	6.2–12.5	1.6–3.1	0.8–1.6	1.6–3.1	9 ± 0.4
Pep13-BP143	6.2–12.5	0.8–1.6	3.1–6.2	0.8–1.6	3.1–6.2	6.2–12.5	8 ± 0.3
BP13-BP16	>50	6.2–12.5	6.2–12.5	12.5–25	>50	>50	86 ± 1.6
BP16-BP13	>50	6.2–12.5	12.5–25	1.6–3.1	25–50	12.5–25	100 ± 2.3

^a*Ea* stands for *Erwinia amylovora*, *Xap* for *Xanthomonas arboricola* pv. pruni, *Xf* for *Xanthomonas fragariae*, *Xav* for *Xanthomonas axonopodis* pv. vesicatoria, *Psa* for *Pseudomonas syringae* pv. actinidiae, *Pss* for *Pseudomonas syringae* pv. syringae.

^bPercent hemolysis at 150 μM plus confidence interval (α = 0.05).

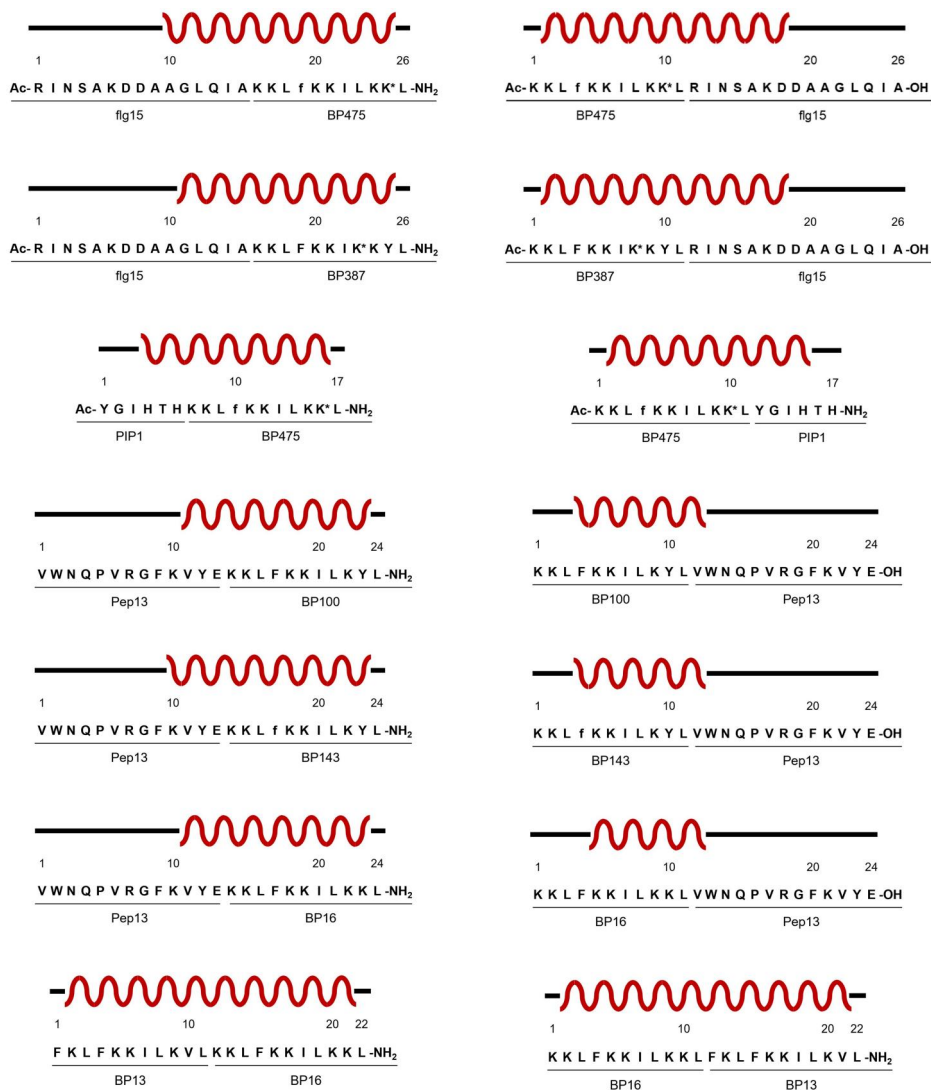


Figure 1. Schematic representation of the secondary structure of peptide conjugates predicted by NMR. Red curves mark the α -helical region and black lines assign residues in a random coil. Lipopeptides **BP475** and **BP387** incorporate a butanoyl group at the side-chain of the lysine with an asterisk. Lowercase letters correspond to *D*-amino acids.

medium range $\alpha N(i, i+2)$, $\alpha N(i, i+3)$ and $\alpha N(i, i+4)$ NOEs were found from residues 12 to 25, typical of an α -helical conformation. Regarding the latter, a weak $\alpha N(i, i+4)$ NOE was observed between Gln¹³ and Lys¹⁷, and strong cross-peaks between Ile¹⁴ and Leu¹⁸, and Ala¹⁵ and *D*-Phe¹⁹.

Peptide conjugates **PIP1-BP475** and **BP475-PIP1** displayed a slightly higher α -helix population (73%) that spans almost the entire sequence. The NOESY spectra of **BP475-PIP1** showed strong medium range $\alpha N(i, i+3)$ NOEs for residues 1 to 14 and a weak $\alpha N(i, i+4)$ NOE between Leu⁸ and Tyr¹².

Concerning the six peptide conjugates that contain the elicitor peptide **Pep13** and the antimicrobial peptide **BP100**, **BP143** or **BP16**, the percentage of α -helix population depended on the position of the latter in the sequence. **Pep13** derivatives with the antimicrobial peptide at the C-terminus showed a higher percentage of α -helix population (68–75%) compared to those with this peptide at the N-terminus (34–50%). In all these six sequences, the helical structure involves mainly the residues of the antimicrobial peptide. These results were confirmed by the NOESY

correlations. In the case of **Pep13-BP100** strong medium range $\alpha N(i, i+3)$ NOEs were found for residues 8 to 22 whereas for **BP100-Pep13** these NOE cross-peaks were observed only for residues 4 to 12.

In the case of the two conjugates containing **BP13**, **BP13-BP16** and **BP16-BP13**, it was determined that they folded into a complete α -helix (88 and 90% of α -helix population, respectively) (Figure 1). The NOESY spectra of **BP13-BP16** revealed a more rigid structure with medium range $\alpha N(i, i+3)$ correlations for all the residues. This spectra also showed $NN(i, i+2)$ and $\alpha N(i, i+4)$ cross-peaks for most of the residues. The same trend was observed for its counterpart **BP16-BP13**.

The secondary structure of these 14 peptide conjugates was also analysed by circular dichroism (CD). The CD spectra were recorded in 30% TFE in 10 mM sodium phosphate buffer at pH 7.4. For all sequences the obtained spectra were characteristic of a typical α -helical conformation with two negative minimum bands at 208 and 222 nm (Supporting Info). These results were in agreement with the above conformational analysis performed by NMR.

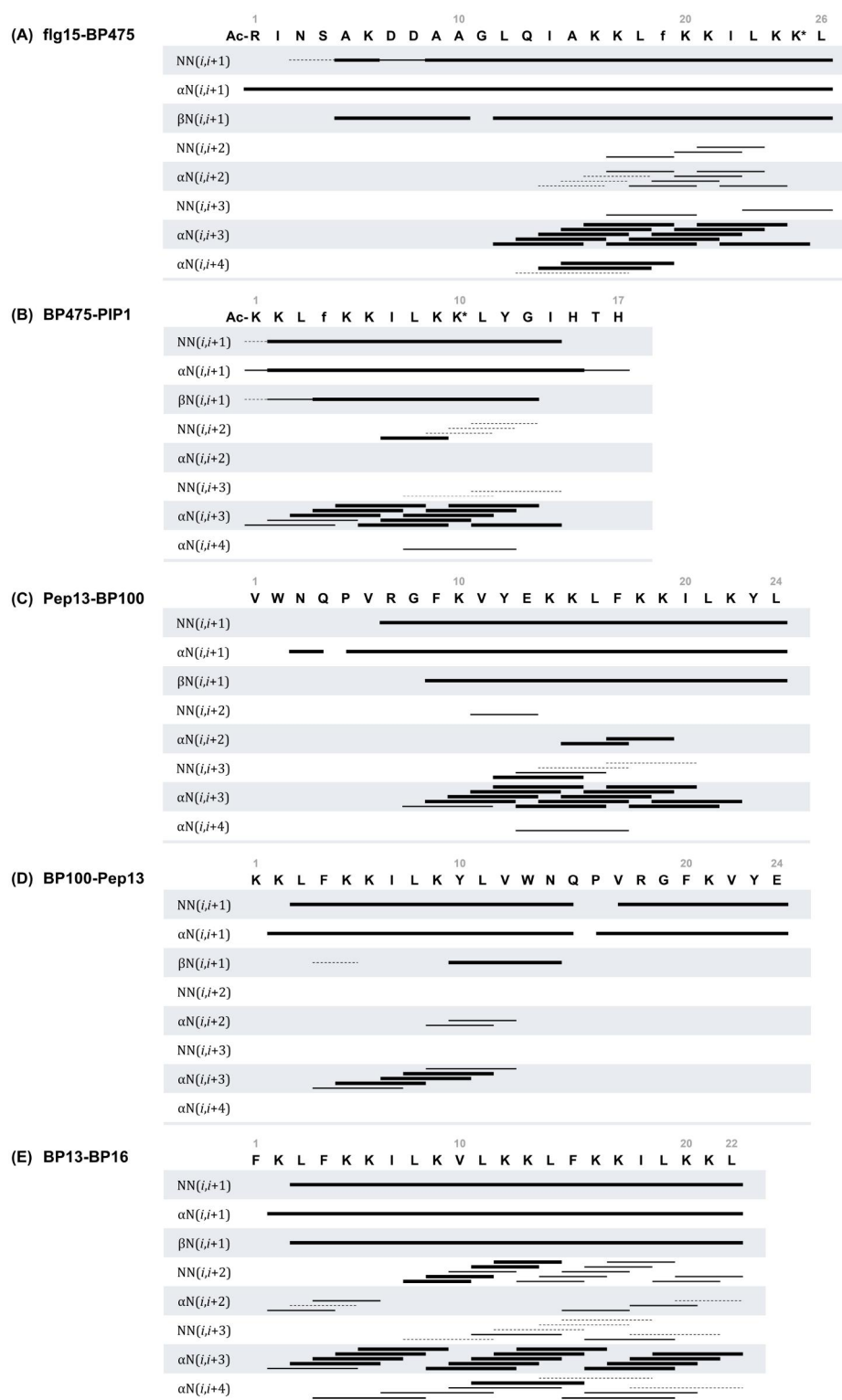


Figure 2. Summary of NOEs for peptide conjugates **flg15-BP475**, **BP475-PIP1**, **Pep13-BP100**, **BP100-Pep13** and **BP13-BP16**. Thickness of lines indicates the intensity of the signal.

2.3. Analysis of the secondary structure of peptide conjugates in micelles

To further corroborate the secondary structure of these peptide conjugates as well as their interaction with lipid membranes, we carried out NMR experiments in presence of anionic SDS- d_{25} and zwitterionic DPC- d_{38} micelles which are well-known models for mimicking membranes. In particular,

we analyzed the peptide conjugates **flg15-BP475**, **BP100-Pep13** and **BP13-BP16** because the two former sequences are among the most active **flg15** and **Pep13** derivatives, respectively, and the latter is one of the least active conjugates.

For this purpose, the 1D and 2D NMR spectra of these selected peptide conjugates were recorded in presence of

the above micelles at 40 °C and the ^1H chemical shifts were assigned. The spectra obtained in SDS- d_{25} micelles were of lower resolution than those in DPC- d_{38} micelles. **Figure 3** shows a bar plot of the chemical shift deviation, $\Delta\delta_{\text{H}\alpha}$, defined as the difference between the experimental $\text{H}\alpha$ chemical shift and the characteristic random coil values, as a function of peptide sequence (Wishart et al., 1995). The data corresponding to the spectra recorded in 30% TFE- d_3 are also included in this figure. The dashed lines in the graphs **A-C** mark the random coil range and bars below this range correspond to residues found in the helical region.

Results showed that peptides adopted similar conformation in both micelles which was in agreement with that observed in TFE- d_3 . Accordingly, in the case of **flg15-BP475** it was found an α -helical region at the C-terminus involving some residues of **flg15** and all the **BP475** fragment (**Figure 3A**). Regarding **BP100-Pep13**, an α -helix was localized at the N-terminus of the conjugate corresponding to BP100, whereas the **Pep13** fragment assumed a random coil conformation (**Figure 3B**). Finally, as previously

observed in TFE- d_3 , **BP13-BP16** folded into an α -helix that spanned throughout the entire sequence with no appreciable differences along the peptide (**Figure 3C**).

The conformation of the three peptides was also analyzed by CD under the same conditions used in the NMR experiments (SDS and DPC micelles, 30% TFE) as well as in aqueous medium. The CD spectra showed that the three peptide conjugates were completely unstructured in water, but they adopted an α -helix structure in presence of micelles or 30% TFE (**Figure 4**). It can be noted, that the CD profile of all three peptides was similar in both conditions. As expected from the NMR results, the intensity of the bands characteristic of an α -helix was higher in the case of the peptide conjugate **BP13-BP16** (**Figure 4C**).

2.4. Study of the localization of the peptide conjugates in micelles

The localization of the peptide conjugates **flg15-BP475**, **BP100-Pep13** and **BP13-BP16** relative to the surface of DPC

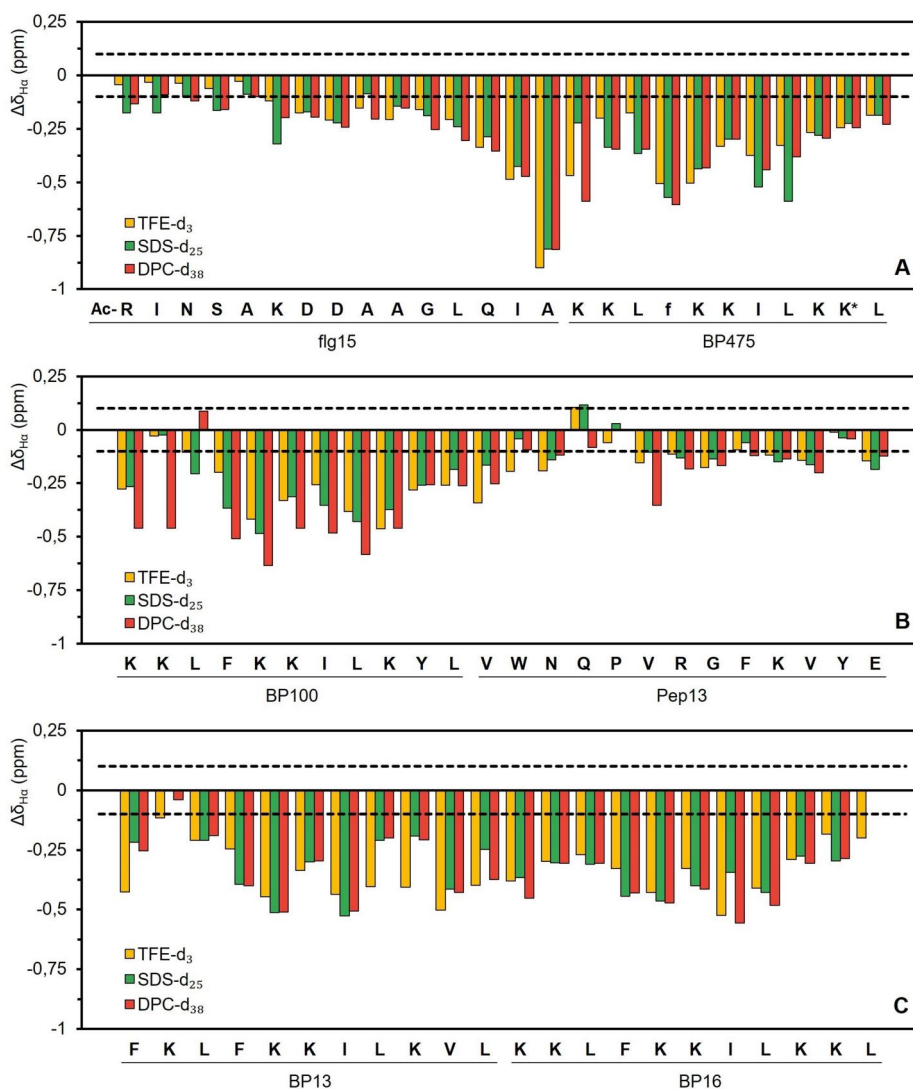


Figure 3. $\Delta\delta_{\text{H}\alpha}$ determined in TFE- d_3 , SDS- d_{25} and DPC- d_{38} for (A) **flg15-BP475**, (B) **BP100-Pep13** and (C) **BP13-BP16**. Dashed lines represent the range of random coil chemical shifts. Lipopeptide **BP475** incorporates a butanoyl group at the side-chain of the lysine with an asterisk. Lowercase letters correspond to D-amino acids.

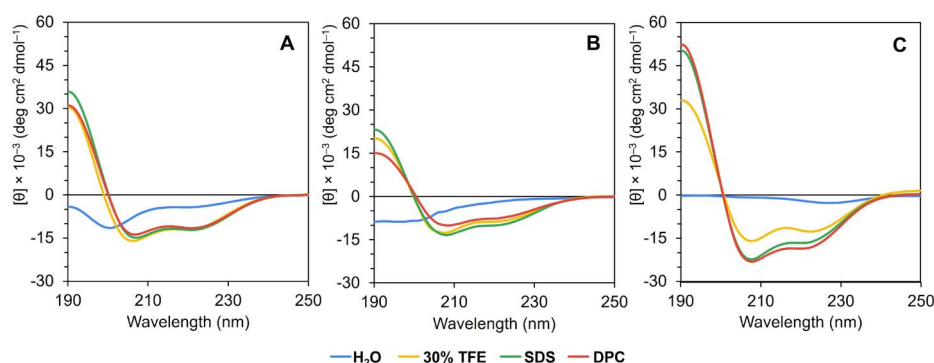


Figure 4. CD spectra of (A) **fig15-BP475**, (B) **BP100-Pep13** and (C) **BP13-BP16** in H₂O, 30% TFE, SDS and DPC micelles.

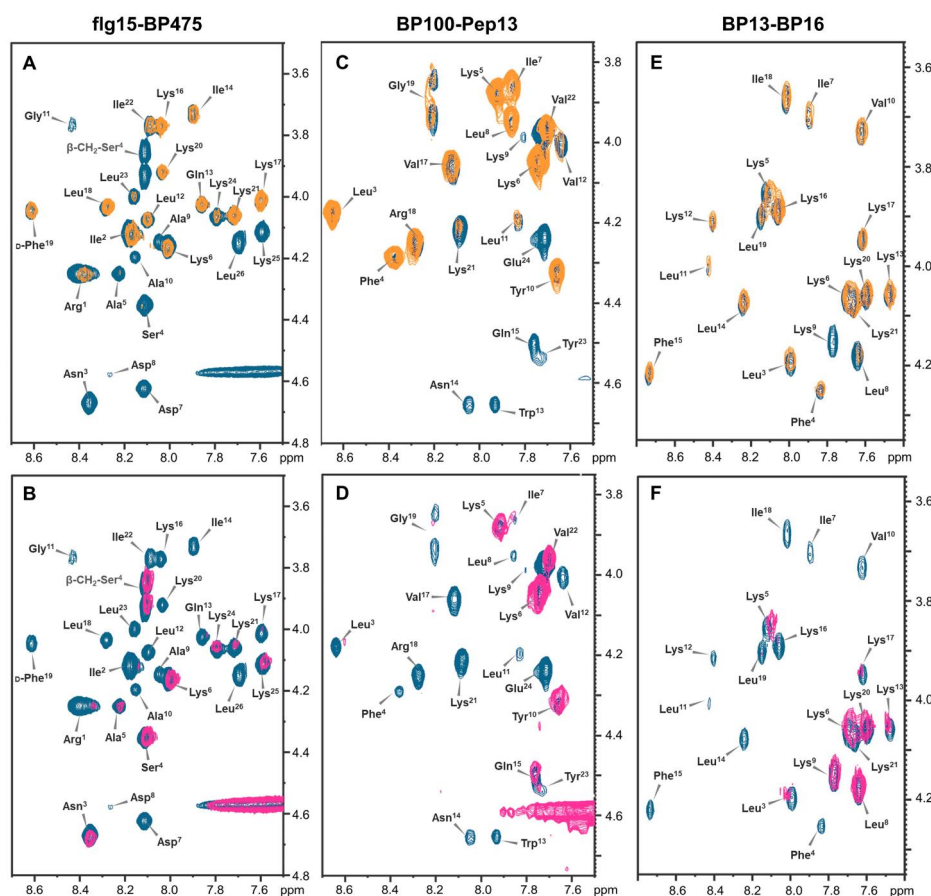


Figure 5. Effect of paramagnetic probes in DPC-d₃₈ micelles. Spectra show H_α/NH TOCSY correlations before the addition of paramagnetic compounds (blue signals) and after the addition of MnCl₂ (orange signals) and 16-DSA (pink signals): **fig15-BP475** with (A) MnCl₂ and (B) 16-DSA, **BP100-Pep13** with (C) MnCl₂ and (D) 16-DSA, and **BP13-BP16** with (E) MnCl₂ and (F) 16-DSA.

micelles was analysed by paramagnetic relaxation enhancement NMR (PRE NMR) experiments using MnCl₂ and 16-doxy stearic acid (16-DSA) as paramagnetic relaxation agents. The water-soluble MnCl₂ selectively suppresses the signals corresponding to the most solvent-exposed residues whereas the liposoluble 16-DSA affects the signals of the membrane-embedded residues. The TOCSY spectra of these peptide conjugates are represented in Figure 5 in which the intensity changes of the H_α/NH cross-peaks of residues were estimated in the absence or in the presence of these paramagnetic probes. In order to quantify the effect of the perturbation caused by paramagnetic compounds and be able to compare between the peptides, we considered the

remaining amplitude, defined as the relation between the intensities of the H_α/NH cross-peaks (H_α/H_δ for Pro residues) in the TOCSY spectrum after and before the addition of these probes (Figure 6).

In the case of **fig15-BP475**, the TOCSY spectra showed that the most affected amino acids by the addition of MnCl₂ were those corresponding to the first half of the sequence (from Asn³ to Gly¹¹) and the two last residues (Lys²⁵ and Leu²⁶) (Figure 5A). Conversely, these amino acids seemed to be the less affected by the addition of the liposoluble 16-DSA (Figure 5B). Accordingly, the quantification of the effect of these probes revealed that the addition of MnCl₂ caused a significant drop of the intensities of the H_α/NH cross-peaks

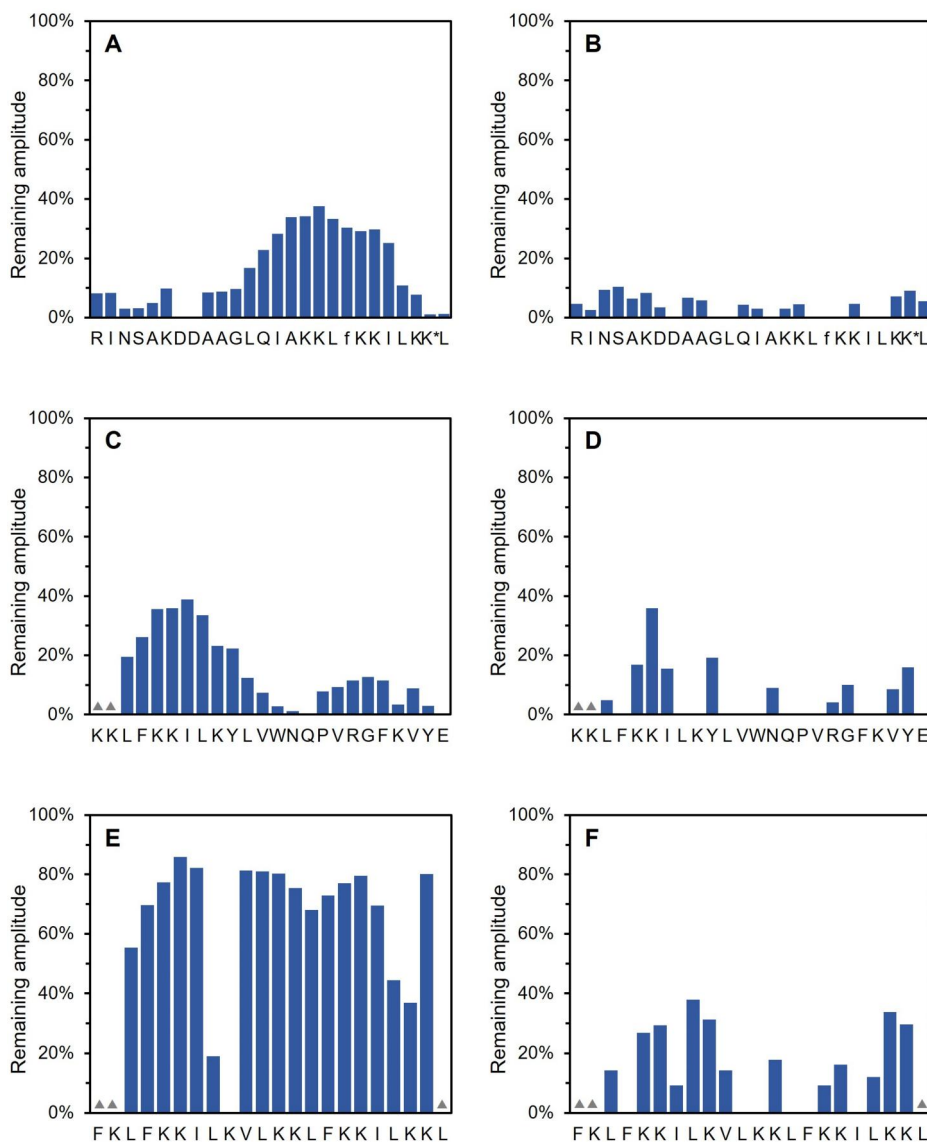


Figure 6. Remaining amplitude of H_{α}/NH cross-peaks for the addition of (A) $MnCl_2$ in **fig15-BP475**, (B) 16-DSA in **fig15-BP475**, (C) $MnCl_2$ in **BP100-Pep13**, (D) 16-DSA in **BP100-Pep13**, (E) $MnCl_2$ in **BP13-BP16** and (F) 16-DSA in **BP13-BP16**. Residues marked with a triangle could not be quantified due to fast exchange with solvent.

of the first 11 amino acids and an increase of the cross-peaks corresponding to amino acids 12 to 24 (Figure 6A). This observation is in agreement with the conformation predicted for this peptide conjugate which adopted an α -helix in the C-terminal region. The formation of this α -helix would stabilize the interactions between the residues in this region, being less solvent-exposed. In contrast, after the addition of 16-DSA a dramatic decrease in the intensity of the H_{α}/NH cross-peaks of all the amino acids of the sequence was observed (Figure 6B). The maximum remaining amplitude was 10%, corresponding to Ser⁴. This result provided evidence that, overall, the peptide significantly interacted with the micelles. It is worth noting that after the addition of 16-DSA, the signals corresponding to the side-chain protons of residues Ala¹⁰ to Leu²⁶ were totally quenched, as inferred from the comparison of the TOCSY spectra. In this spectrum, the signals of β -CH₂-Ser⁴ and β -CH₂-Lys⁶ were still observed after the addition of this probe, reinforcing that the N-terminus of **fig15-BP475** was less absorbed in the micelles.

Regarding the peptide conjugate **BP100-Pep13**, the amino acids of the first half of the sequence (Leu³ to Tyr¹⁰) were the least affected by the addition of $MnCl_2$ and exhibited higher remaining amplitude values of the H_{α}/NH cross-peaks than the rest of the residues (Figure 6C). These observations are in agreement with the secondary structure adopted by this peptide conjugate, with the N-terminus folding into an α -helix. The addition of 16-DSA resulted in an overall decrease of the intensity of all signals and only some particular H_{α}/NH cross-peaks remained (Figure 5D). Similarly to **fig15-BP475**, the addition of the paramagnetic probes had an important effect in the signals corresponding to the side chain of the amino acids. For instance, among the lysine residues present in this peptide, only the C-terminal Lys²¹ did not show a TOCSY correlation between H_{α} and H_{ϵ} in $MnCl_2$, as expected for a more solvent-exposed residue.

Concerning **BP13-BP16**, the addition of $MnCl_2$ caused a low decrease of the intensity of the H_{α}/NH cross-peaks, 14 amino acids exhibited remaining amplitude values >60%

(Figure 6E). This is in agreement with an α -helix spanned throughout the entire sequence, as predicted. Furthermore, the addition of 16-DSA quenched the signals of residues from both the N- and the C-terminus. However, compared with the above peptide conjugates, a considerable number of signals with higher remaining amplitude were detected, suggesting that the insertion of **BP13-BP16** into the micelles was weaker.

2.5. Computational prediction of the structure and conformational dynamics of peptide conjugates

Peptides are dynamic and can exist as an ensemble of multiple conformations that can be important for activity and protein and membrane recognition. To gain insight into the structure and conformational dynamics of the peptide conjugates, we explored their conformational ensemble with molecular dynamics (MD) simulations in explicit solvent. To this end, we selected two groups of peptides that present different structure-activity relationships based on the NMR assignments and experimental activity assays: a) highly active **Pep13-BP100** and **BP100-Pep13** peptides where the **BP100** segment present helical character and **Pep13** is mainly disordered; and b) less active **BP13-BP16** and **BP16-BP13** peptides that according to NMR present a collective helical character.

To explore the conformational ensemble of the selected peptide conjugates, we applied a computational protocol that consists of the following steps. First, we used deep learning-based AlphaFold2 (Jumper et al., 2021) to generate initial models of the 3D structure of the selected peptide conjugates. Second, these 3D models were used as a starting point for MD simulations. To extensively explore the conformational space and access the time scales typical of protein folding, we performed enhanced sampling simulations with Gaussian accelerated molecular dynamics (GaMD) (Miao et al., 2015). The GaMD trajectories were analyzed to reconstruct the conformational landscape of the peptide conjugates as a function of the RMSD with respect to the AlphaFold2 structure (indicator of global flexibility) and the radius of gyration (indicator of peptide compactness) of the protein. Finally, this conformational landscape was clustered using hierarchical agglomerative clustering as implemented in cptraj (Roe & Cheatham, 2013) to obtain the most relevant conformational states and its relative populations.

In **BP100-Pep13**, the predicted AlphaFold2 structure assigned an alpha helical character to residues 2-13 and a disordered structure to the 14-24 segment (see Figure 7a). This computational prediction was in line with NMR assignments. The conformational landscape generated from GaMD simulations in explicit solvent indicated that **BP100-Pep13** can sample a wide range of conformations (Figure 7b and c). In general, the helical character of the **BP100** fragment was mostly preserved while **Pep13** was intrinsically flexible and can adopt multiple disordered orientations either bending toward the **BP100** section (more populated) or adopting more extended conformation (less populated). The presence

of Pro¹⁶ and Gly¹⁹ in the **Pep13** fragment played a key role in keeping this region unstructured and highly dynamic. In the most populated conformation (Cluster 1 in Figure 7c), hydrophobic interactions between residues located in the folded and unfolded sections were observed, keeping most of the lysine residues solvent exposed. Interestingly, the **BP100** fragment can transiently unfold (Cluster 4 in Figure 7c) but rapidly came back to the folded state. Peptide conjugate **Pep13-BP100** presented a similar behavior keeping the helical character in the **BP100** fragment. The conformational plasticity of these two **Pep13**-containing peptide conjugates may play a role in recognizing and binding membranes (see below).

In the case of **BP16-BP13**, AlphaFold2 predicted a continuous helical structure for the 2-21 segment including both **BP16** and **BP13** regions (see Figure 7d), which perfectly matched the NMR assignment. In comparison to **BP100-Pep13**, the conformational landscape of **BP16-BP13** obtained from GaMD simulations was more restricted in terms of global flexibility (see Figure 7e and f). In the most populated cluster (Cluster 1 in Figure 7f), the central part of the **BP16-BP13** (residues 5-19) retained the helical structure with all charged lysines pointing in the same direction. Transiently, the helix was splitted into two parts by a short turn that coincided with the interface between the **BP16** and **BP13** fragments. Overall, MD simulations showed that **BP16-BP13** conjugates were significantly less flexible than **BP100-Pep13**, which may impact the interactions with the membrane and, consequently, its activity.

2.6. Molecular basis of peptide-membrane interactions

To evaluate the molecular basis of the interaction between peptide conjugates and bacterial membranes and its potential impact on the membrane integrity, we performed 500 ns GaMD simulations of **BP100-Pep13** and **BP16-BP13** in the presence of a membrane composed of anionic DPPG lipids (see Figure 8). All simulations started with the peptide conjugate placed 10 Å away from the membrane surface allowing the free diffusion of the peptide from the solvent to the membrane. From these simulations, we compared the process of molecular recognition and the subsequent interaction and orientation with respect to the membrane for both peptides. The GaMD simulations indicated different interaction patterns in **BP100-Pep13** and **BP16-BP13** that were caused by the different structural features which may have important implications for activity.

In the **BP100-Pep13** GaMD simulations, the peptide recognition was driven by the lysine residues Lys¹, Lys², Lys⁵, Lys⁶, and Lys⁹, which rapidly established transient salt bridge interactions with the phosphate groups of DPPG lipids (see Figure 8a). In this orientation, most of the non-charged residues pointed toward the solvent. Once the recognition had taken place, the **BP100** fragment folded and unfolded when interacting with the membrane, indicating that its helical character can be altered in contact with the membrane. The **Pep13** fragment remained unfolded during the simulation and transiently interacted with the membrane. After 250 ns,

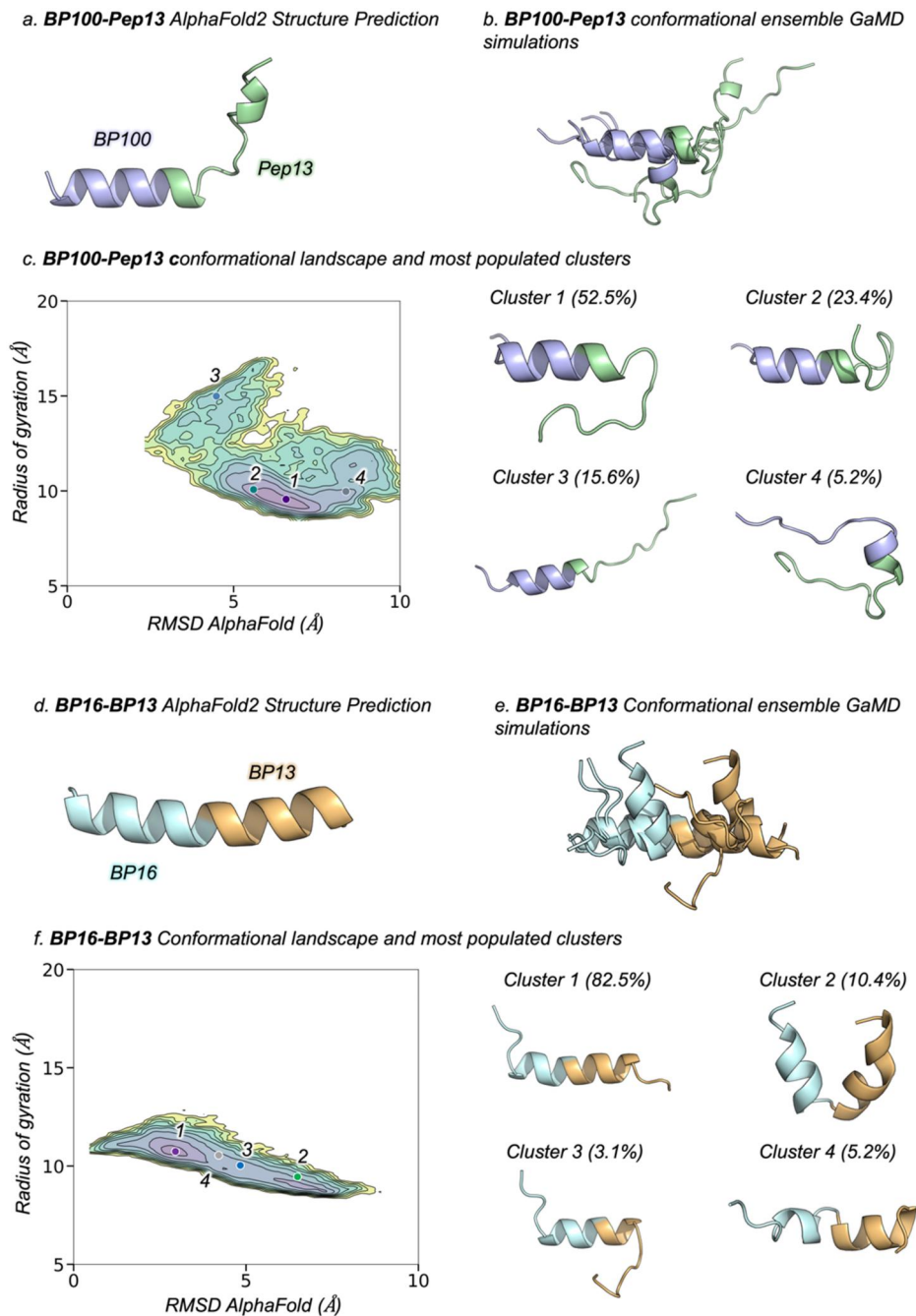
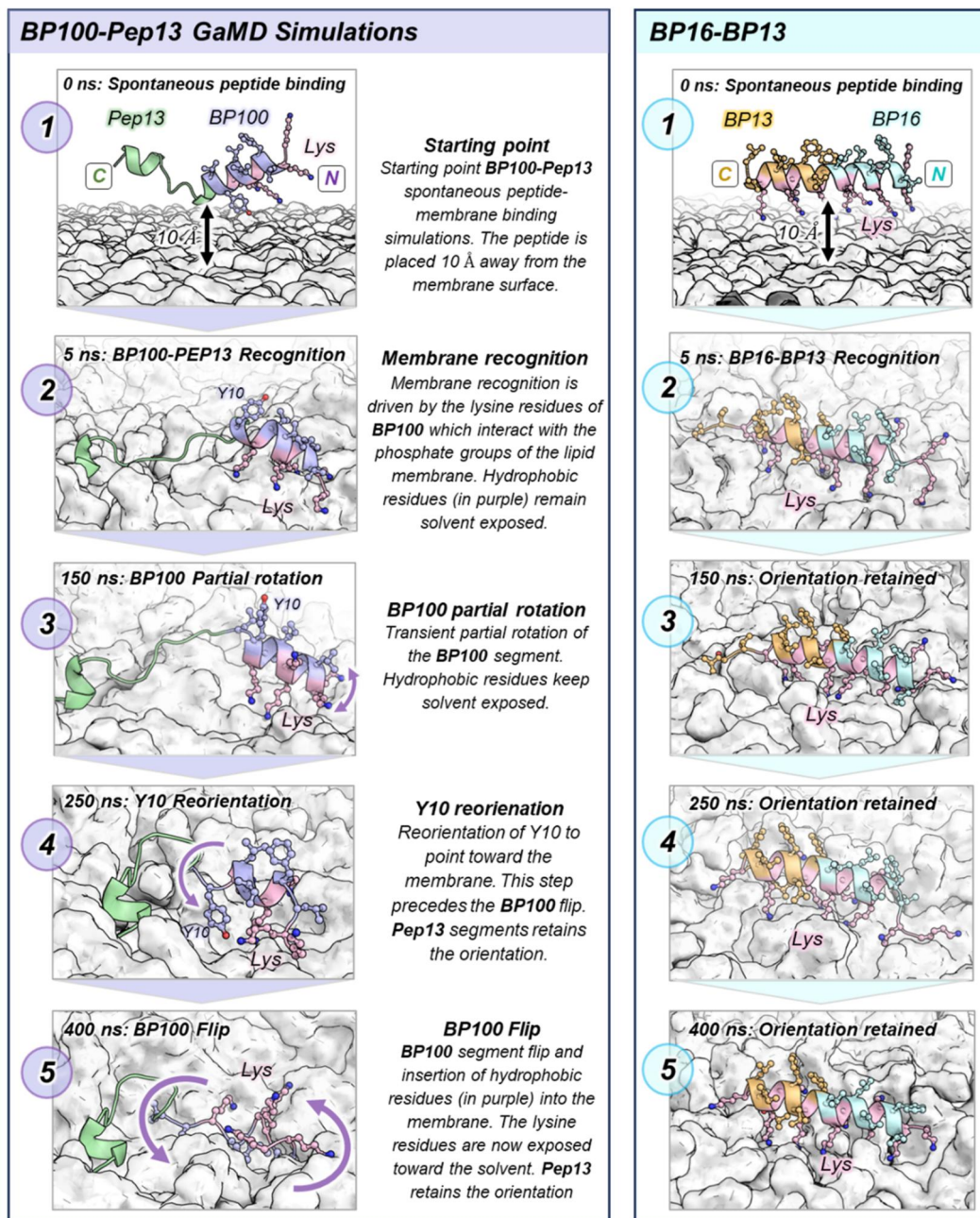


Figure 7. Conformational ensemble of BP100-Pep13 and BP16-BP13. a) Highest ranked conformation of BP100-Pep13 predicted with AlphaFold2. The BP100 and Pep13 segments are shown in purple and green, respectively. b) Overlay of the five most populated clusters obtained from the 3 replicas of 200 ns of GaMD simulations of BP100-Pep13. c) Conformational landscape of BP100-Pep13 as a function of the RMSD with respect to the AlphaFold2 structure (in Å) and the radius of gyration (in Å) and structures and populations of the four most populated clusters. In the conformational landscape, the most populated regions are depicted in purple while the less populated are shown in yellow. The position of the most populated clusters is represented in spheres in the plot. d) Highest ranked conformation of BP16-BP13 predicted with AlphaFold2. The BP16 and BP13 segments are shown in cyan and orange, respectively. e) Overlay of the five most populated clusters obtained from the 3 replicas of 200 ns of GaMD simulations of BP16-BP13. f) Conformational landscape of BP16-BP13 as a function of the RMSD with respect to the AlphaFold2 structure (in Å) and the radius of gyration (in Å) and structures and populations of the four most populated clusters. In the conformational landscape, the most populated regions are depicted in purple while the less populated are shown in yellow. The position of the most populated clusters is represented in spheres in the plot.

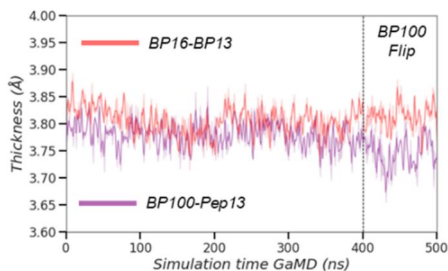
Tyr¹⁰ reorients to point toward the membrane (see Figure 8a). This reorientation precedes a series of changes that result in the BP100 flip. More precisely, after 400 ns of GaMD simulation time, some interactions between the lysines and the membrane were broken and the BP100 fragment was able to flip its orientation. This flip was characterized by the non-charged residues pointing toward the

membrane while the charged lysines interacted with the solvent. This peptide flip induced the insertion of the peptide into the membrane, which involved the thinning of the membrane around the peptide (see Figure 8b). In this way, the non-polar side-chains of Leu³, Ile⁷, and Tyr¹⁰ could be stabilized by the lipid tails. This orientation was preserved during the remaining simulation time.

a. Molecular mechanism of peptide-membrane interactions



b. Membrane Thickness



c. Membrane Curvature Angle

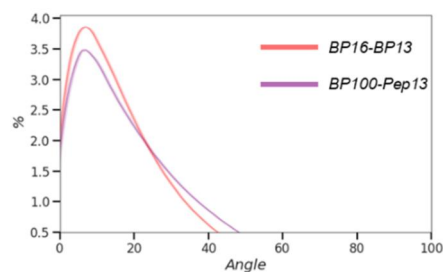


Figure 8. Molecular mechanism of peptide-membrane interactions. a) Time evolution of BP100-Pep13 and BP16-BP13 interactions with DPPG anionic membranes obtained from 500 ns GaMD simulations. The key steps observed for each peptide-membrane system are depicted and briefly described. Lysines are shown in pink, hydrophobic residues of BP100 fragment are shown in purple, BP16 in cyan, and BP13 in orange. b) Time evolution of membrane thickness calculated with the SuAVE software. BP100-Pep13 is colored in purple while BP16-BP13 in red. c) Probability distribution of membrane curvature angles calculated with the SuAVE software. BP100-Pep13 is colored in purple while BP16-BP13 in red.

On the other hand, GaMD simulations showed that **BP16-BP13** followed a similar recognition pattern than **BP100-Pep13**. Once the peptide was recognized by the membrane, the peptide was placed in a parallel orientation with respect to the membrane with Lys¹, Lys², Lys⁵, Lys⁶, Lys⁹, and Lys¹⁰ from **BP16** and Lys¹³ and Lys¹⁶ from **BP13** establishing salt bridge interactions with the phosphate groups. In general, the peptide retained the helical character when interacting with the membrane indicating that its helicity was preserved. In contrast to **BP100-Pep13**, the peptide flip was not observed during the simulation, keeping the lysine residues interacting with the anionic phosphate groups of the membrane surface. These results indicated that the flip of **BP16-BP13** was prevented or significantly slowed down with respect to **BP100-Pep13** keeping the conjugated peptide in the membrane surface. By comparing the sequence of the **BP100** and **BP16** fragments, the only difference is in position 10, which is occupied by a tyrosine in **BP100** and by a lysine in **BP16**. MD simulations showed that the interaction of Tyr¹⁰ with the membrane was key to induce and stabilize the flipped orientation in **BP100-Pep13** while, in the case of **BP16-BP13**, Lys¹⁰ prevented the reorientation because it helped to stabilize the orientation with lysine residues interacting with the phosphate groups. In comparison to **BP100-Pep13**, **BP16-BP13** do not alter the thickness of the membrane and show a lower membrane angle curvature (see Figure 8b and c).

3. Discussion

The good biological properties against plant pathogens of peptide conjugates previously identified in our group (Oliveras et al., 2022) prompted us to investigate the relationship between their structural characteristics and their biological activity to obtain insights for designing new sequences with enhanced properties. These peptide conjugates resulted from the combination of **BP100** or a **BP100** derivative (**BP16**, **BP143**, **BP387** or **BP475**) with a plant defence elicitor peptide (**flg15**, **BP13**, **Pep13** or **PIP1**). Fourteen peptide conjugates were chosen: twelve highly or moderately active sequences with low hemolysis and two low active and highly hemolytic. NMR was used to analyze their secondary structure and micelle localization, and computational studies were employed to explore their conformational ensembles and the molecular basis of their membrane interactions. The results revealed a correlation between the conformation of the peptides, their interaction with membranes, and their biological activity.

Analysis of the structure of these peptide conjugates by NMR techniques in 30% TFE-d₃ allowed to classify the peptides with high and moderate activity into 3 groups according to their α -helix population. The first group included the four peptide conjugates containing the elicitor peptide **flg15** and the antimicrobial peptide **BP387** or **BP475**. These sequences exhibited an α -helix population ranging from 62 to 69%. In this secondary structure the residues of the antimicrobial peptide, regardless of its position in the conjugate, adopted an α -helix while the residues corresponding to **flg15**

remained as a random coil as confirmed by the NOESY spectra. In the second group we found **PIP1-BP475** and **BP475-PIP1** with a higher α -helix population (73%) that involves almost all the residues of the sequence. The third group comprised the six peptide conjugates bearing the elicitor peptide **Pep13** and the antimicrobial peptides **BP100**, **BP143** or **BP16**. In this case the position of the antimicrobial peptide influenced the percentage of α -helix, being higher (68–75%) for those sequences with the antimicrobial peptide at the C-terminus compared to the derivatives with the antimicrobial peptide at the N-terminus (68–75% vs. 34–50%). Regarding the two peptide conjugates **BP13-BP16** and **BP16-BP13** that exhibited the lowest antibacterial activity and the highest hemolysis, they showed a more rigid structure with almost all the entire sequence folded into an α -helix (88% and 90% α -helix population, respectively). CD analysis in 30% TFE supported the NMR results, showing characteristic α -helical spectra with negative minimum bands at 208 and 222 nm for all 14 peptide conjugates. Therefore, the percentage of α -helix population depends on the elicitor peptide present in the sequence, **flg15**, **Pep13** or **PIP1** mostly adopting a random coil and **BP13** a rigid α -helix.

The above-described results confirm the hypothesis postulated in our previous study on this family of peptide conjugates (Oliveras et al., 2022), specially regarding the importance of the secondary structure on the antibacterial and hemolytic activities. Thus, a percentage of α -helix population together with the presence of a flexible random coil fragment renders peptide conjugates with high activity and low hemolysis (**flg15**, **Pep13** and **PIP1** derivatives) whereas a rigid α -helix structure has an unfavorable effect both on the antibacterial and hemolytic activities (**BP13** derivatives). Apart from the secondary structure, other important parameters that govern the biological activity of these peptide conjugates are the cationicity, hydrophobicity and amphipathicity. Notably, a balance between these parameters is required for an optimal biological activity profile as previously reported (Huang & Li, 2023; Jiang et al., 2020; Oliveras et al., 2022). Accordingly, the best peptide conjugates (**flg15**, **Pep13** and **PIP1** derivatives) have a positive charge between +5 and +7, and a moderate hydrophobic moment/amphipathic character. In contrast, poorly active and high hemolytic sequences (**BP13** derivatives) have a positive charge of +10 and a considerably higher hydrophobicity and amphipathicity.

The α -helix structure found in our peptide conjugates could confer them with the ability to target bacterial membranes. Thus, we further carried out NMR and CD experiments to determine the structure of three representative peptide conjugates (**flg15-BP475**, **BP100-Pep13** and **BP13-BP16**) in anionic SDS and zwitterionic DPC micelles, which have been commonly used as membrane mimics to study the structure of antimicrobial peptides (Bischetti et al., 2023; Gomes et al., 2018; Kao et al., 2022; Porcelli et al., 2006; Sani & Separovic, 2016; Shenkarev et al., 2011; Usachev et al., 2015; Wu et al., 2020). The secondary structures of **flg15-BP475**, **BP100-Pep13** and **BP13-BP16** determined from NMR and CD experiments in the presence of SDS and DPC

micelles were consistent with those obtained with TFE. Moreover, similar conformations in both micelles were obtained. In general terms, the antimicrobial fragment of **flg15-BP475** and **BP100-Pep13** folded into a helical structure whereas almost all the sequence of **BP13-BP16** adopted an α -helix. Examples of antimicrobial peptides that are similarly structured in SDS and DPC micelles can be found in the literature, such as the piscidin antimicrobial peptide **Of-Pis1** and the methicillin-resistant *Staphylococcus aureus*-inhibiting antimicrobial peptide **RR14** (Bischetti et al., 2023; Kao et al., 2022). However, conformational differences have also been observed for other antimicrobial peptides depending on the micelle composition. This is the case of ocellatin-F1 that forms a more linear α -helix in SDS than in DPC (Gomes et al., 2018).

Besides the secondary structure, the localization and orientation of peptides within membrane environments are related to their mechanism of action. Investigation of the spatial arrangement of an antimicrobial peptide can lead to the identification of functionally essential fragments that can be rationally modified to obtain peptides with improved antimicrobial activity. With this in mind, we explored the localization of the three peptide conjugates **flg15-BP475**, **BP100-Pep13** and **BP13-BP16** in DPC-d₃₈ micelles. We selected these micelles, because the spectra recorded in them resulted more resolved with well-dispersed cross-peaks than in SDS-d₂₅ micelles. Analysis of the localization of these three peptide conjugates relative to the surface of DPC micelles using PRE NMR experiments in presence of MnCl₂ and 16-DSA revealed that **flg15-BP475** and **BP100-Pep13** significantly interacted with the micelles, and that their interaction was stronger than that of **BP13-BP16**. In addition, the results obtained were consistent with the secondary structure adopted by these peptide conjugates described above. In the case of **flg15-BP475** and **BP100-Pep13**, the water-soluble paramagnetic probe MnCl₂ significantly affected amino acids that are not involved in the α -helical structure with a noticeable decrease in intensity of the corresponding H α /NH cross-peaks. Moreover, the addition of this probe led to an increase of the cross-peak intensity for the amino acids that adopt an α -helix. Conversely, the liposoluble paramagnetic probe 16-DSA caused a significant decrease of all the amino acid signals. These results align with the predicted α -helix conformation in the C-terminal region for **flg15-BP475**, suggesting a significant interaction of this region with micelles, whereas the N-terminus is less membrane-embedded. For **BP100-Pep13**, results are consistent with an α -helix in the N-terminus and a more solvent-exposed C-terminus. Finally, **BP13-BP16** exhibited a minor decrease in H α /NH cross-peak intensity in the presence of MnCl₂, aligning with the predicted α -helix spanning the entire sequence. Moreover, 16-DSA quenched signals from both termini, with a higher number of signals showing a high remaining amplitude, indicating a weaker interaction with micelles compared to the other peptide conjugates.

Even though NMR experiments on DPC micelles provide high-resolution structures, these structural results need to be complemented with MD simulations, which constitute a

better approximation to the behaviour of the peptide in cell membranes. In addition, these simulations may give further clues about the location and orientation of peptides in the lipidic membranes. MD simulations in explicit solvent were conducted with one of the least active peptides (**BP16-BP13**) together with two of the most active peptides, one of them bearing **BP100** at the N-terminus (**BP100-Pep13**) and the other one with **BP100** at the C-terminus (**Pep13-BP100**). In general, the structures obtained in these GaMD simulations were in line with the NMR assignments. These simulations also revealed that peptide conjugates **BP100-Pep13** and **Pep13-BP100** adopted various conformations exhibiting higher intrinsic flexibility than **BP16-BP13**. Thus, a high flexibility seems to be crucial for the antibacterial activity of these conjugates.

GaMD simulations of **BP100-Pep13** and **BP16-BP13** in the presence of a membrane composed of anionic DPPG lipids were also in agreement with the above features and, additionally, showed that the helical **BP100** fragment is responsible for the antibacterial activity of **BP100-Pep13**. In fact, residues Lys¹, Lys², Lys⁵, Lys⁶, Lys⁹ and Tyr¹⁰ of **BP100** allowed the electrostatic attraction of this conjugate with the membrane and, then, its insertion into the membrane. **BP100-Pep13** was first oriented parallel to the membrane with the non-charged residues of the **B100** fragment exposed to the solvent and the positively charged lysines (Lys¹, Lys², Lys⁵, Lys⁶, Lys⁹) faced towards the membrane and interacting with the negative phosphate groups of the DPPG lipids. The **Pep13** fragment appeared flexible adopting multiple disordered structures folded towards **BP100** or in an extended form. After disruption of some lysine interactions with the membrane, the orientation of the **BP100** α -helix changed, leaving the lysine side chains exposed to the solvent and the hydrophobic amino acids Leu³, Ile⁷ and Tyr¹⁰ faced towards the membrane and prompting the insertion of the peptide. Interestingly, Tyr¹⁰ plays a key role in this mechanism as it was concluded by analyzing the GaMD simulations of the non-active peptide conjugate **BP16-BP13**. This Tyr¹⁰ contributes to the flipping of **BP100-Pep13** and to maintain this flipped orientation, which could be directly associated with the high antibacterial activity of this peptide. In contrast, in the case of **BP16-BP13** all the sequence is oriented parallel to the membrane and all the charged lysines are involved in the electrostatic attraction of this peptide with the membrane. Unlike **BP100-Pep13**, the lysine at position 10 together with the other lysines of **BP13** prevented the reorientation of **BP16-BP13**, leading to a lower antibacterial activity.

Flexibility is another key determining factor for the antibacterial activity of membrane-active peptides besides cationicity, hydrophobicity and amphipathicity (Babii et al., 2017; Liu et al., 2013). A balance between rigidity and flexibility is required for an optimal activity. Based on the above, the intrinsic flexibility and less charged character of **BP100-Pep13** facilitated the interaction of non-charged or less bulky residues such as Leu³, Ile⁷, or Tyr¹⁰ with the membrane while in the case of **BP16-BP13** only charged and long lysine residues remained faced toward the membrane. The fact that

BP100-Pep13 was able to flip facilitating the interactions of non-charged residues with the membrane seemed key to trigger the insertion into the membrane and its thinning. On the other hand, the restricted conformational plasticity of **BP16-BP13** and the higher number of positively charged residues may slow down the insertion to the membrane affecting peptide activity. This mode of action is also in accordance with the mechanism of action previously reported for **BP100**. This antimicrobial peptide was also described to bind flat to the membrane surface, with the lysine residues oriented towards the bilayer, followed by a flip, which leads to the insertion of the hydrophobic face of **BP100** into the membrane (Franco et al., 2022; Park et al., 2019; Strandberg et al., 2023).

4. Conclusions

Taken together our data can be drawn that the antibacterial activity of membrane-active peptides depends not only on factors like cationicity, hydrophobicity, and amphipathicity but also on flexibility. Achieving an optimal level of activity requires a delicate balance between rigidity and flexibility. The inherent flexibility and moderate cationicity of **BP100-Pep13** facilitate its flipping, which seems to enhance its interaction with the membrane, promoting peptide insertion and causing membrane thinning. This behaviour correlates with the high activity exhibited by this peptide conjugate. These results provide guidelines for future rational design of **BP100** derivatives.

5. Materials and methods

5.1. NMR

Structural characterization of peptide conjugates was determined by NMR spectroscopy. NMR spectra were acquired at the Serveis Tècnics de Recerca of the University of Girona with a Ultrashield 400 MHz spectrometer from Bruker equipped with a RT BBI and processed and analyzed using TopSpin 3.6.2.

For the experiments carried out in presence of 2,2,2-trifluoroethanol- d_3 (TFE- d_3), the corresponding peptide conjugate (4 mM) was dissolved in 20 mM phosphate buffer at pH 6.5 in H_2O/D_2O (90:10) containing 30% of TFE- d_3 . Each peptide conjugate was analyzed with the following experiments: 1D 1H -NMR; 2D 1H - 1H TOCSY (mixing time = 80 ms); 2D 1H - 1H NOESY (mixing time = 400 ms); 2D 1H - ^{13}C multiplicity-edited HSQC; 2D 1H - ^{15}N HSQC and 2D 1H - ^{13}C HSQC-TOCSY. All spectra were acquired at 313 K and water suppression was achieved with excitation sculpting or the Watergate scheme. From NMR experiments, the 1H , ^{13}C and ^{15}N - chemical shifts were assigned following the standard sequential assignment approach (Wüthrich, 1986) and structural determination was determined by Chemical Shift Index 3.0 web server (Berjanskii & Wishart, 2005, 2008; Hafsa et al., 2015).

For the experiments in presence of micelles, the peptide conjugate (1.5 mM) was dissolved in 10% D_2O at pH 3.5 in presence of 60 mM perdeuterated sodium dodecyl sulphate

(SDS- d_{25}) or perdeuterated dodecylphosphocholine (DPC- d_{38}). The following experiments were recorded at 313 K: 1D 1H -NMR; 2D 1H - 1H COSY, 2D 1H - 1H TOCSY (mixing time = 80 ms) and 2D 1H - 1H NOESY (mixing time = 400 ms). In all cases, sodium 2,2-dimethyl-2-silapentane-5-sulfonate (DSS) was used as internal reference for 1H chemical shifts.

To assess the localization of the peptide conjugates relative to the surface of DPC micelles, paramagnetic relaxation enhancement (PRE) experiments were performed by acquiring 1D 1H -NMR and 2D 1H - 1H TOCSY experiments either in the absence and the presence of 1.5 mM $MnCl_2$ as a water-soluble paramagnetic agent and 1.5 mM 16-doxyl-stearic acid (16-DSA) as a lipid-soluble paramagnetic probe. For the latter, the 16-DSA stock solution was prepared in MeOD. The effect of the presence of the paramagnetic agent on each residue was quantified by means of the remaining amplitude, which was calculated according to the ratio between the intensities of the H_{α}/NH cross-peaks (H_{α}/H_{δ} for Pro residues) in the TOCSY spectrum after and before the addition of the paramagnetic agent (Pandit et al., 2018).

$$\text{remaining amplitude} = \frac{I_{H_{\alpha}/NH} \text{ (paramagnetic agent)}}{I_{H_{\alpha}/NH} \text{ (without paramagnetic agent)}}$$

5.2. Circular dichroism spectroscopy

CD spectra were recorded in the Centres Científics i Tecnològics of the Universitat de Barcelona using a Jasco J-815 spectropolarimeter from Jasco International Co. All experiments were recorded at a wavelength between 190 and 250 nm using a quartz cuvette with 1 mm optical path. The spectra were measured at a scan rate of 50 nm/min with a bandwidth of 0.5 nm, a response time of 1 s and taking an accumulation of three scans at 298 K. Samples were prepared at a concentration of 100 μM under different conditions: (i) in a 10 mM phosphate buffer at pH 6.5, (ii) in phosphate buffer containing 30% TFE, (iii) in presence of 30 mM of SDS micelles, and (iv) in presence of 30 mM of DPC micelles. Data was processed with the Jasco Spectra Analysis software and the calculation of the mean residue ellipticity, $[\theta]$, was performed as previously reported (Rajasekaran et al., 2019) and expressed in mdeg $cm^2 dmol^{-1}$ units.

5.3. Gaussian molecular dynamics simulations

Gaussian Molecular Dynamics (MD) simulations of the peptide conjugates **BP100-Pep13**, **Pep13-BP100**, **BP16-BP13**, and **BP13-BP16** in the absence of membrane and **BP100-Pep13** and **BP16-BP13** in the presence of an anionic DPPG lipid membrane were performed using the AMBER20 MD package (Case et al., 2020). The amino acid residues of the conjugated peptides were modelled with the force field Amber ff14SB (Maier et al., 2015), the anionic DPPG lipids with the SLipid force-field (Jämbeck & Lyubartsev, 2012), and explicit TIP3P (Jorgensen et al., 1983) water molecules were considered to solvate the system.

5.3.1. Modelling and simulation strategy

The starting point of the GaMD simulations for the **BP100-Pep13**, **Pep13-BP100**, **BP16-BP13**, and **BP13-BP16** were built using AlphaFold2 (Jumper et al., 2021). These initial models were subjected to three replicas of 200 ns of GaMD simulations. These trajectories were collectively analysed to reconstruct the conformational landscape of the peptide conjugates as a function of the RMSD with respect to the AlphaFold2 structure (indicator of global flexibility) and the radius of gyration (indicator of peptide compactness) of the protein. In more detail, we calculated the RMSD and radius of gyration for each frame of the GaMD trajectories and we represented these values using a 2D-kernel-density plot using PyEMMA software (Scherer et al., 2015), the most populated regions are depicted in purple while the less populated are shown in yellow. Finally, this conformational landscape was clusterized using hierarchical agglomerative clustering as implemented in cpptraj (Roe & Cheatham, 2013) to obtain the most relevant conformational states and its relative populations. The most populated clusters of GaMD simulations for **BP100-Pep13** and **BP16-BP13** were selected as starting points for peptide-membrane simulations. The lipid bilayer to simulate the conjugated peptide-membrane systems was prepared with CHARMM-Gui web server (Jo et al., 2008; Wu et al., 2014) using a lipid area of 100 Å × 100 Å of anionic DPPG lipids (including 160 lipids in each leaflet) with 0.15 M concentration of NaCl considering a neutralized system. The peptide was situated 10 Å away from the membrane surface to allow the free diffusion during the initial steps of the GaMD simulation.

5.3.2. Molecular dynamics and GaMD simulations

In the case of the conjugated peptides in the absence of the lipid bilayer, we conducted the MD simulations using the following strategy. Before starting the MD simulations, a two-stage geometry optimization approach was performed. First, a short minimization of the positions of water molecules with positional restraints on the solute by a harmonic potential with a force constant of 500 kcal mol⁻¹Å⁻² was done. The second stage consists of an unrestrained minimization of all the atoms in the simulation cell. Then, the systems were heated in six 50 ps steps, increasing the temperature by 50 K each step (0 – 300K) under constant-volume, periodic-boundary conditions, and the particle-mesh Ewald approach (Darden et al., 1993) to introduce long-range electrostatic effects. A 10 Å cutoff was applied to Lennard-Jones and electrostatic interactions during the process. Bonds involving hydrogen were constrained with the SHAKE algorithm. Harmonic restraints of 10 kcal mol⁻¹ were applied to the solute, and the Langevin equilibration scheme was used to control and equalize the temperature. The timestep was kept at 2 fs during the heating stages, allowing potential inhomogeneities to self-adjust. Each system was then equilibrated for 2 ns with a 2 fs time step at a constant pressure of 1 atm (NPT ensemble). Finally, 100 ns of conventional MD trajectories at a constant volume and temperature (300 K) were carried out. From this structure we performed unconstrained gaussian accelerated molecular dynamics (GaMD) simulations

(Miao et al., 2015). GaMD is an unconstrained enhanced sampling technique that enhances conformational sampling by applying a harmonic boost potential to flatten the energy landscape. The GaMD simulations were performed using the AMBER package. First, a 10 ns conventional MD simulations was carried out to calculate the GaMD acceleration parameters. Second, a 50 ns GaMD equilibration run was performed. Third, 3 independent replicas of 200 ns of ‘dual-boost’ GaMD were carried out for **BP100-Pep13**, **Pep13-BP100**, **BP16-BP13**, and **BP13-BP16**. The reference energy was set to the upper bound (as described above) and the upper limit of the boost potential standard deviation, σ_0 , was set to 6.0 kcal/mol.

The MD simulations of **BP100-Pep13** and **BP16-BP13** in the presence of a DPPG lipid bilayer were performed with the AMBER package using the CHARMM-GUI suggested protocol. First, a short minimization of the whole system with positional restraints on the peptide and membrane was carried out that was followed by six equilibration steps of 250 ps in the isotropic NPT ensemble using the Berendsen barostat progressively reducing the positional restraints of both peptide and membrane. Next, 5 ns of MD simulations in the NPT ensemble without positional restraints are performed. From this, the GaMD protocol is applied. First, a 10 ns conventional MD simulations was carried out to calculate the GaMD acceleration parameters. Second, a 50 ns GaMD equilibration run was performed. Third, 500 ns of ‘dual-boost’ GaMD were carried out for **BP100-Pep13** and **BP16-BP13**. The GaMD simulations were performed at the same conditions as described before. The SuAVE software has been used to monitor the membrane thickness and membrane curvature angle along the GaMD simulations (Santos et al., 2020).

Acknowledgements

We acknowledge the Serveis Tècnics de Recerca of the University of Girona for the NMR experiments.

Disclosure statement

No potential conflict of interest was reported by the authors.

Funding

This research was funded by grants RTI2018-099410-B-C22 (MICINN/AEI/FEDER, UE) and PID2022-140040B-C22 (MCIN/AEI/10.13039/501100011033/FEDER, UE). G.R.-L. was recipient of a fellowship from the University of Girona. F.F. thanks Generalitat de Catalunya AGAUR for 2021SGR00487 and the Spanish MINECO for RYC2020-029552-I and PID2022-141676NB-I00.

Data availability statement

The data supporting the findings of this study can be found in both the main text and the ESI.

References

- Babii, O., Afonin, S., Schober, T., Komarov, I. V., & Ulrich, A. S. (2017). Flexibility vs rigidity of amphipathic peptide conjugates when interacting with lipid bilayers. *Biochimica et Biophysica Acta, Biomembranes*, 1859(12), 2505–2515. <https://doi.org/10.1016/j.bbmem.2017.09.021>
- Badosa, E., Ferre, R., Planas, M., Feliu, L., Besalú, E., Cabrefiga, J., Bardají, E., & Montesinos, E. (2007). A library of linear undecapeptides with bactericidal activity against phytopathogenic bacteria. *Peptides*, 28(12), 2276–2285. <https://doi.org/10.1016/j.peptides.2007.09.010>
- Badosa, E., Planas, M., Feliu, L., Montesinos, L., Bonaterra, A., & Montesinos, E. (2022). Synthetic peptides against plant pathogenic bacteria. *Microorganisms*, 10(9), 1784. <https://doi.org/10.3390/microorganisms10091784>
- Berjanskii, M. V., & Wishart, D. S. (2005). A simple method to predict protein flexibility using secondary chemical shifts. *Journal of the American Chemical Society*, 127(43), 14970–14971. <https://doi.org/10.1021/ja054842f>
- Berjanskii, M. V., & Wishart, D. S. (2008). Application of the random coil index to studying protein flexibility. *Journal of Biomolecular NMR*, 40(1), 31–48. <https://doi.org/10.1007/s10858-007-9208-0>
- Bischetti, M., Alaimo, N., Nardelli, F., Punzi, P., Amarié, C., Ingenito, R., Musco, G., Gallo, M., & Cicero, D. O. (2023). Structural insights on the selective interaction of the histidine-rich piscidin antimicrobial peptide Of-Pis1 with membranes. *Biochimica et Biophysica Acta, Biomembranes*, 1865(1), 184080. <https://doi.org/10.1016/j.bbmem.2022.184080>
- Buck, M. (1998). Trifluoroethanol and colleagues: Cosolvents come of age. Recent studies with peptides and proteins. *Quarterly Reviews of Biophysics*, 31(3), 297–355. <https://doi.org/10.1017/S003358359800345X>
- Case, D. A., Belfon, K., Ben-Shalom, I. Y., Brozell, S. R., Cerutti, D. S., Cheatham, III, T. E., Cruzeiro, V. W. D., Darden, T. A., Duke, R. E., Giambasu, M. K., Gilson, H., Gohlke, A. W., Goetz, R., Harris, S., Izadi, S. A., Izmailov, K., Kasavajhala, A., Kovalenko, R., Krasny, T., ... Kollman, P. A. (2020). *AMBER 2020*. University of California.
- Chen, C. H., & Lu, T. K. (2020). Development and challenges of antimicrobial peptides for therapeutic applications. *Antibiotics*, 9(1), 24. <https://doi.org/10.3390/antibiotics9010024>
- Ciumac, D., Gong, H., Hu, X., & Lu, J. R. (2019). Membrane targeting cationic antimicrobial peptides. *Journal of Colloid and Interface Science*, 537, 163–185. <https://doi.org/10.1016/j.jcis.2018.10.103>
- Darden, T., York, D., & Pedersen, L. (1993). Particle mesh Ewald: An N²-log(N) method for Ewald sums in large systems. *The Journal of Chemical Physics*, 98(12), 10089–10092. <https://doi.org/10.1063/1.464397>
- Devi, N., Singh, P., Sharma, R., Kumar, M., Pandey, S. K., Sharma, R. K., & Wangoo, N. (2022). A lysine-rich cell penetrating peptide engineered multifunctional gold nanoparticle-based drug delivery system with enhanced cellular penetration and stability. *Journal of Materials Science*, 57(35), 16842–16857. <https://doi.org/10.1007/s10853-022-07681-z>
- Eales, M. G., Ferrari, E., Goddard, A. D., Lancaster, L., Sanderson, P., & Miller, C. (2018). Mechanistic and phenotypic studies of bicarinalin, BP100 and colistin action on *Acinetobacter baumannii*. *Research in Microbiology*, 169(6), 296–302. <https://doi.org/10.1016/j.resmic.2018.04.005>
- Eggenberger, K., Mink, C., Wadhvani, P., Ulrich, A. S., & Nick, P. (2011). Using the peptide Bp100 as a cell-penetrating tool for the chemical engineering of actin filaments within living plant cells. *ChemBiochem: A European Journal of Chemical Biology*, 12(1), 132–137. <https://doi.org/10.1002/cbic.201000402>
- Erdem Büyükkiraz, M., & Kesmen, Z. (2022). Antimicrobial peptides (AMPs): A promising class of antimicrobial compounds. *Journal of Applied Microbiology*, 132(3), 1573–1596. <https://doi.org/10.1111/jam.15314>
- Franco, L. R., Park, P., Chaimovich, H., Coutinho, K., Cuccovia, I. M., & Lima, F. S. (2022). Simulations reveal that antimicrobial BP100 induces local membrane thinning, slows lipid dynamics and favors water penetration. *RSC Advances*, 12(8), 4573–4588. <https://doi.org/10.1039/D1RA06267K>
- Gomes, K. A. G. G., dos Santos, D. M., Santos, V. M., Piló-Veloso, D., Mundim, H. M., Rodrigues, L. V., Lião, L. M., Verly, R. M., de Lima, M. E., & Resende, J. M. (2018). NMR structures in different membrane environments of three ocellatin peptides isolated from *Leptodactylus labyrinthicus*. *Peptides*, 103, 72–83. <https://doi.org/10.1016/j.peptides.2018.03.016>
- Grage, S. L., Afonin, S., Kara, S., Buth, G., & Ulrich, A. S. (2016). Membrane thinning and thickening induced by membrane-active amphipathic peptides. *Frontiers in Cell and Developmental Biology*, 4, 65. <https://doi.org/10.3389/fcell.2016.00065>
- Hafsa, N. E., Arndt, D., & Wishart, D. S. (2015). CSI 3.0: A web server for identifying secondary and super-secondary structure in proteins using NMR chemical shifts. *Nucleic Acids Research*, 43(W1), W370–W377. <https://doi.org/10.1093/nar/gkv494>
- Huang, X., & Li, G. (2023). Antimicrobial peptides and cell-penetrating peptides: Non-antibiotic membrane-targeting strategies against bacterial infections. *Infection and Drug Resistance*, 16, 1203–1219. <https://doi.org/10.2147/IDR.S396566>
- Jämbeck, J. P. M., & Lyubartsev, A. P. (2012). An extension and further validation of an all-atomistic force field for biological membranes. *Journal of Chemical Theory and Computation*, 8(8), 2938–2948. <https://doi.org/10.1021/ct300342n>
- Jiang, Y., Mei, C., Huang, X., Gu, Q., & Song, D. (2020). Antibacterial activity and mechanism of a bacteriocin derived from the valine-cecropin A(1–8)-plantaricin ZJ5(1–18) hybrid peptide against *Escherichia coli* O104. *Food Biophysics*, 15(4), 442–451. <https://doi.org/10.1007/s11483-020-09636-w>
- Jo, S., Kim, T., Iyer, V. G., & Im, W. (2008). CHARMM-GUI: A web-based graphical user interface for CHARMM. *Journal of Computational Chemistry*, 29(11), 1859–1865. <https://doi.org/10.1002/jcc.20945>
- Jorgensen, W. L., Chandrasekhar, J., Madura, J. D., Impey, R. W., & Klein, M. L. (1983). Comparison of simple potential functions for simulating liquid water. *The Journal of Chemical Physics*, 79(2), 926–935. <https://doi.org/10.1063/1.445869>
- Jumper, J., Evans, R., Pritzel, A., Green, T., Figurnov, M., Ronneberger, O., Tunyasuvunakool, K., Bates, R., Židek, A., Potapenko, A., Bridgland, A., Meyer, C., Kohl, S. A. A., Ballard, A. J., Cowie, A., Romera-Paredes, B., Nikolov, S., Jain, R., Adler, J., ... Hassabis, D. (2021). Highly accurate protein structure prediction with AlphaFold. *Nature*, 596(7873), 583–589. <https://doi.org/10.1038/s41586-021-03819-2>
- Kao, C.-C., Lin, T.-L., Lin, C.-J., & Tseng, T.-S. (2022). Deciphering structure-function relationship unveils salt-resistant mode of action of a potent MRSA-inhibiting antimicrobial peptide, RR14. *Journal of Bacteriology*, 204(12), e0031222. <https://doi.org/10.1128/jb.00312-22>
- Lei, J., Sun, L. C., Huang, S., Zhu, C., Li, P., He, J., Mackey, V., Coy, D. H., & He, Q. Y. (2019). The antimicrobial peptides and their potential clinical applications. *American Journal of Translational Research*, 11(7), 3919–3931.
- Li, J., Koh, J.-J., Liu, S., Lakshminarayanan, R., Verma, C. S., & Beuerman, R. W. (2017). Membrane active antimicrobial peptides: Translating mechanistic insights to design. *Frontiers in Neuroscience*, 11, 73. <https://doi.org/10.3389/fnins.2017.00073>
- Liu, L., Fang, Y., & Wu, J. (2013). Flexibility is a mechanical determinant of antimicrobial activity for amphipathic cationic α -helical antimicrobial peptides. *Biochimica et Biophysica Acta*, 1828(11), 2479–2486. <https://doi.org/10.1016/j.bbmem.2013.06.017>
- Liu, Y., Shi, J., Tong, Z., Jia, Y., Yang, B., & Wang, Z. (2021). The revitalization of antimicrobial peptides in the resistance era. *Pharmacological Research*, 163, 105276. <https://doi.org/10.1016/j.phrs.2020.105276>
- Lobo, F., & Boto, A. (2022). Host-defense peptides as new generation phytosanitaries: Low toxicity and low induction of antimicrobial resistance. *Agronomy*, 12(7), 1614. <https://doi.org/10.3390/agronomy12071614>
- Luo, X., Chen, H., Song, Y., Qin, Z., Xu, L., He, N., Tan, Y., & Dessie, W. (2023). Advancements, challenges and future perspectives on peptide-based drugs: Focus on antimicrobial peptides. *European Journal of Pharmaceutical Sciences: Official Journal of the European Federation*

- for *Pharmaceutical Sciences*, 181, 106363. <https://doi.org/10.1016/j.ejps.2022.106363>
- Magana, M., Pushpanathan, M., Santos, A. L., Leanse, L., Fernandez, M., Ioannidis, A., Giulianotti, M. A., Apidianakis, Y., Bradfute, S., Ferguson, A. L., Cherkasov, A., Seleem, M. N., Pinilla, C., de la Fuente-Nunez, C., Lazaridis, T., Dai, T., Houghten, R. A., Hancock, R. E. W., & Tegos, G. P. (2020). The value of antimicrobial peptides in the age of resistance. *The Lancet. Infectious Diseases*, 20(9), e216–e230. [https://doi.org/10.1016/S1473-3099\(20\)30327-3](https://doi.org/10.1016/S1473-3099(20)30327-3)
- Mahlapuu, M., Björn, C., & Ekblom, J. (2020). Antimicrobial peptides as therapeutic agents: Opportunities and challenges. *Critical Reviews in Biotechnology*, 40(7), 978–992. <https://doi.org/10.1080/07388551.2020.1796576>
- Maier, J. A., Martinez, C., Kasavajhala, K., Wickstrom, L., Hauser, K. E., & Simmerling, C. (2015). ff14SB: Improving the accuracy of protein side chain and backbone parameters from ff99SB. *Journal of Chemical Theory and Computation*, 11(8), 3696–3713. <https://doi.org/10.1021/acs.jctc.5b00255>
- Mercurio, F. A., Scaloni, A., Caira, S., & Leone, M. (2019). The antimicrobial peptides casocidins I and II: Solution structural studies in water and different membrane-mimetic environments. *Peptides*, 114, 50–58. <https://doi.org/10.1016/j.peptides.2018.09.004>
- Miao, Y., Feher, V. A., & McCammon, J. A. (2015). Gaussian accelerated molecular dynamics: Unconstrained enhanced sampling and free energy calculation. *Journal of Chemical Theory and Computation*, 11(8), 3584–3595. <https://doi.org/10.1021/acs.jctc.5b00436>
- Miyamoto, T., Toyooka, K., Chuah, J.-A., Odahara, M., Higuchi-Takeuchi, M., Goto, Y., Motoda, Y., Kigawa, T., Kodama, Y., & Numata, K. (2022). A synthetic multidomain peptide that drives a macropinosytosis-like mechanism for cytosolic transport of exogenous proteins into plants. *JACS Au*, 2(1), 223–233. <https://doi.org/10.1021/jacsau.1c00504>
- Oddo, A., Thomsen, T. T., Kjelstrup, S., Gorey, C., Franzyk, H., Frimodt-Møller, N., Løbner-Olesen, A., & Hansen, P. R. (2016). An amphipathic undecapeptide with all D-amino acids shows promising activity against colistin-resistant strains of acinetobacter baumannii and a dual mode of action. *Antimicrobial Agents and Chemotherapy*, 60(1), 592–599. <https://doi.org/10.1128/AAC.01966-15>
- Oliveras, À., Camó, C., Caravaca-Fuentes, P., Moll, L., Riesco-Llach, G., Gil-Caballero, S., Badosa, E., Bonaterra, A., Montesinos, E., Feliu, L., & Planas, M. (2022). Peptide conjugates derived from flg15, Pep13, and PIP1 that are active against plant-pathogenic bacteria and trigger plant defense responses. *Applied and Environmental Microbiology*, 88(12), e0057422. <https://doi.org/10.1128/aem.00574-22>
- Pandit, G., Ilyas, H., Ghosh, S., Bidkar, A. P., Mohid, S. A., Bhunia, A., Satpati, P., & Chatterjee, S. (2018). Insights into the mechanism of antimicrobial activity of seven-residue peptides. *Journal of Medicinal Chemistry*, 61(17), 7614–7629. <https://doi.org/10.1021/acs.jmedchem.8b00353>
- Park, P., Franco, L. R., Chaimovich, H., Coutinho, K., Cuccovia, I. M., & Lima, F. S. (2019). Binding and flip as initial steps for BP-100 antimicrobial actions. *Scientific Reports*, 9(1), 8622. <https://doi.org/10.1038/s41598-019-45075-5>
- Porcelli, F., Buck-Koehntop, B. A., Thennarasu, S., Ramamoorthy, A., & Veglia, G. (2006). Structures of the dimeric and monomeric variants of magainin antimicrobial peptides (MSI-78 and MSI-594) in micelles and bilayers, determined by NMR spectroscopy. *Biochemistry*, 45(18), 5793–5799. <https://doi.org/10.1021/bi0601813>
- Rajasekaran, G., Kumar, S. D., Yang, S., & Shin, S. Y. (2019). The design of a cell-selective fowlicidin-1-derived peptide with both antimicrobial and anti-inflammatory activities. *European Journal of Medicinal Chemistry*, 182, 111623. <https://doi.org/10.1016/j.ejmech.2019.111623>
- Roe, D. R., & Cheatham, T. E. (2013). PTRAJ and CPPTRAJ: Software for processing and analysis of molecular dynamics trajectory data. *Journal of Chemical Theory and Computation*, 9, 3084–3095. <https://doi.org/10.1021/ct400341p>
- Sani, M. A., & Separovic, F. (2016). How membrane-active peptides get into lipid membranes. *Accounts of Chemical Research*, 49(6), 1130–1138. <https://doi.org/10.1021/acs.accounts.6b00074>
- Santiveri, C. M., Pantoja-Uceda, D., Rico, M., & Angeles Jiménez, M. (2005). β -hairpin formation in aqueous solution and in the presence of trifluoroethanol: A ^1H and ^{13}C nuclear magnetic resonance conformational study of designed peptides. *Biopolymers*, 79(3), 150–162. <https://doi.org/10.1002/bip.20345>
- Santos, D. E. S., Pontes, F. J. S., Lins, R. D., Coutinho, K., & Soares, T. A. (2020). SuAVE: A Tool for analyzing curvature-dependent properties in chemical interfaces. *Journal of Chemical Information and Modeling*, 60(2), 473–484. <https://doi.org/10.1021/acs.jcim.9b00569>
- Scherer, M. K., Trendelkamp-Schroer, B., Paul, F., Pérez-Hernández, G., Hoffmann, M., Plattner, N., Wehmeyer, C., Prinz, J. H., & Noé, F. (2015). PyEMMA 2: A software package for estimation, validation, and analysis of Markov models. *Journal of Chemical Theory and Computation*, 11(11), 5525–5542. <https://doi.org/10.1021/acs.jctc.5b00743>
- Shenkarev, Z. O., Balandin, S. V., Trunov, K. I., Paramonov, A. S., Sukhanov, S. V., Barsukov, L. I., Arseniev, A. S., & Ovchinnikova, T. V. (2011). Molecular mechanism of action of β -hairpin antimicrobial peptide arenicin: Oligomeric structure in dodecylphosphocholine micelles and pore formation in planar lipid bilayers. *Biochemistry*, 50(28), 6255–6265. <https://doi.org/10.1021/bi200746t>
- Sönnichsen, F. D., Van Eyk, J. E., Hodges, R. S., & Sykes, B. D. (1992). Effect of trifluoroethanol on protein secondary structure: An NMR and CD study using a synthetic actin peptide. *Biochemistry*, 31(37), 8790–8798. <https://doi.org/10.1021/bi00152a015>
- Souza, F. R., Fornasier, F., Carvalho, A. S., Silva, B. M., Lima, M. C., & Pimentel, A. S. (2020). Polymer-coated gold nanoparticles and polymeric nanoparticles as nanocarrier of the BP100 antimicrobial peptide through a lung surfactant model. *Journal of Molecular Liquids*, 314, 113661. <https://doi.org/10.1016/j.molliq.2020.113661>
- Strandberg, E., Wadhvani, P., Bürck, J., Anders, P., Mink, C., van den Berg, J., Ciriello, R. A. M., Melo, M. N., Castanho, M. A. R. B., Bardaji, E., Ulmschneider, J. P., & Ulrich, A. S. (2023). Temperature-dependent realignment of the short multifunctional peptide BP100 in membranes revealed by solid-state NMR spectroscopy and molecular dynamics simulations. *ChemBiochem: A European Journal of Chemical Biology*, 24(4), e202200602. <https://doi.org/10.1002/cbic.202200602>
- Talapko, J., Meštrović, T., Juzbašić, M., Tomas, M., Erić, S., Horvat Aleksijević, L., Bekić, S., Schwarz, D., Matić, S., Neuberger, M., & Škrlec, I. (2022). Antimicrobial peptides—mechanisms of action, antimicrobial effects and clinical applications. *Antibiotics*, 11(10), 1417. <https://doi.org/10.3390/antibiotics11101417>
- Torres, L. M. F. C., Almeida, M. T., Santos, T. L., Marinho, L. E. S., de Mesquita, J. P., da Silva, L. M., dos Santos, W. T. P., Martins, H. R., Kato, K. C., Alves, E. S. F., Liao, L. M., de Magalhães, M. T. Q., de Mendonça, F. G., Pereira, F. V., Resende, J. M., Bemquerer, M. P., Rodrigues, M. A., & Verly, R. M. (2019). Antimicrobial alumina nano-biostructures of disulfide- and triazole-linked peptides: Synthesis, characterization, membrane interactions and biological activity. *Colloids and Surfaces B: Biointerfaces*, 177, 94–104. <https://doi.org/10.1016/j.colsurfb.2019.01.052>
- Usachev, K. S., Efimov, S. V., Kolosova, O. A., Filippov, A. V., & Klochkov, V. V. (2015). High-resolution NMR structure of the antimicrobial peptide protegrin-2 in the presence of DPC micelles. *Journal of Biomolecular NMR*, 61(3–4), 227–234. <https://doi.org/10.1007/s10858-014-9885-4>
- Vila, R., Ponte, I., Suau, P., Jiménez, M. A., & Rico, M. (2000). A helix-turn motif in the C-terminal domain of histone H1. *Protein Science: A Publication of the Protein Society*, 9(4), 627–636. <https://doi.org/10.1110/ps.9.4.627>
- Wadhvani, P., Strandberg, E., van den Berg, J., Mink, C., Bürck, J., Ciriello, R. A. M., & Ulrich, A. S. (2014). Dynamical structure of the short multifunctional peptide BP100 in membranes. *Biochimica et Biophysica Acta*, 1838(3), 940–949. <https://doi.org/10.1016/j.bbame.2013.11.001>
- Wang, Y., Zhao, T., Wei, D., Strandberg, E., Ulrich, A. S., & Ulmschneider, J. P. (2014). How reliable are molecular dynamics simulations of membrane active antimicrobial peptides? *Biochimica et Biophysica Acta*, 1838(9), 2280–2288. <https://doi.org/10.1016/j.bbame.2014.04.009>
- Wishart, D. S., Bigam, C. G., Holm, A., Hodges, R. S., & Sykes, B. D. (1995). ^1H , ^{13}C and ^{15}N random coil NMR chemical shifts of the common amino acids. I. Investigations of nearest-neighbor effects. *Journal of Biomolecular NMR*, 5(1), 67–81. <https://doi.org/10.1007/BF00227471>

- Wishart, D. S., Sykes, B. D., & Richards, F. M. (1991). Relationship between nuclear magnetic resonance chemical shift and protein secondary structure. *Journal of Molecular Biology*, 222(2), 311–333. [https://doi.org/10.1016/0022-2836\(91\)90214-Q](https://doi.org/10.1016/0022-2836(91)90214-Q)
- Wu, E. L., Cheng, X., Jo, S., Rui, H., Song, K. C., Dávila-Contreras, E. M., Qi, Y., Lee, J., Monje-Galvan, V., Venable, R. M., Klauda, J. B., & Im, W. (2014). CHARMM-GUI Membrane Builder toward realistic biological membrane simulations. *Journal of Computational Chemistry*, 35(27), 1997–2004. <https://doi.org/10.1002/jcc.23702>
- Wu, P.-S., Lai, S.-J., Fung, K.-M., & Tseng, T.-S. (2020). Characterization of the structure–function relationship of a novel salt-resistant antimicrobial peptide, RR12. *RSC Advances*, 10(40), 23624–23631. <https://doi.org/10.1039/D0RA04299D>
- Wüthrich, K. (1986). *NMR of proteins and nucleic acids*. Wiley.
- Xuan, J., Feng, W., Wang, J., Wang, R., Zhang, B., Bo, L., Chen, Z.-S., Yang, H., & Sun, L. (2023). Antimicrobial peptides for combating drug-resistant bacterial infections. *Drug Resistance Updates: Reviews and Commentaries in Antimicrobial and Anticancer Chemotherapy*, 68, 100954. <https://doi.org/10.1016/j.drug.2023.100954>
- Yilmaz, N., Kodama, Y., & Numata, K. (2021). Lipid membrane interaction of peptide/DNA complexes designed for gene delivery. *Langmuir: The ACS Journal of Surfaces and Colloids*, 37(5), 1882–1893. <https://doi.org/10.1021/acs.langmuir.0c03320>
- Zamora-Carreras, H., Maestro, B., Strandberg, E., Ulrich, A. S., Sanz, J. M., & Jiménez, M. Á. (2015). Micelle-triggered β -hairpin to α -helix transition in a 14-residue peptide from a choline-binding repeat of the pneumococcal autolysin LytA. *Chemistry – A European Journal*, 21(22), 8076–8089. <https://doi.org/10.1002/chem.201500447>
- Zamora-Carreras, H., Strandberg, E., Mühlhäuser, P., Bürck, J., Wadhvani, P., Jiménez, M. Á., Bruix, M., & Ulrich, A. S. (2016). Alanine scan and 2H NMR analysis of the membrane-active peptide BP100 point to a distinct carpet mechanism of action. *Biochimica et Biophysica Acta*, 1858(6), 1328–1338. <https://doi.org/10.1016/j.bbamem.2016.03.014>
- Zhang, B., Shi, W., Li, J., Liao, C., Yang, L., Huang, W., & Qian, H. (2017). Synthesis and biological evaluation of novel peptides based on antimicrobial peptides as potential agents with antitumor and multidrug resistance-reversing activities. *Chemical Biology & Drug Design*, 90(5), 972–980. <https://doi.org/10.1111/cbdd.13023>